CHARACTERIZATION OF FLOCS AND FLOC SIZE DISTRIBUTIONS USING IMAGE ANALYSIS

A Thesis

Presented to the Faculty of the Graduate School

of Cornell University

in Partial Fulfillment of the Requirements for the Degree of

Master of Science

by

Siwei Sun

February 2016

©2016 Siwei Sun

ABSTRACT

A nonintrusive digital imaging process was developed to study particle size distributions created through flocculation and sedimentation. This process was calibrated by measuring standardized polystyrene particles of known size and was utilized to count and measure individual kaolin clay particles as well as aggregates formed by coagulation with polyaluminum chloride and flocculation. Identification of out-of focus flocs was automated with LabVIEW and used to remove them from the database that was analyzed. The particle diameter of the test suspension of kaolinite clay was measured to be 7.7±3.8 μm and a linear relationship was obtained between turbidity and the concentration of clay particles determined by imaging. The analysis technique was applied to characterize flocs and floc particle size distribution as a function of coagulant dose. Removal of flocs by sedimentation was characterized by imaging and the negative logarithm of the fraction of turbidity remaining after settling had a positive linear association with the logarithm of aluminum dose. The maximum floc size observed in the settled water was less than 120 μm, which was in accordance with the value predicted by a terminal velocity model for the capture velocity of the experimental tube settler of 0.21 mm/s.

BIOGRAPHICAL SKETCH

Siwei Sun was born in Shanghai, China in 1990. She graduated with a degree in Environmental Science and Engineering from Shanghai Jiao Tong University in 2013. In college, she was a member of a student group BLUE SKY and worked to enhance public environment consciousness. Her experiences in the environmental field include a half-year internship in Toray Advanced Materials Research Laboratories (China) and a two-year lab research on membranes with Dr. Lina Chi. In September 2013, she entered Cornell University and started her study towards the M.S. Degree in Environmental Engineering.

ACKNOWLEDGMENTS

This thesis is the product of the efforts of many people. First, I would like to thank Dr. Monroe Weber-Shirk and Dr. Len Lion for their guidance and encouragement in the research. Their support was critical to my work. I acknowledge the inspirational instruction of Dr. Monroe Weber-Shirk. He has spent considerable time teaching me about the process of research inquiry. I must also thank Dr. Len Lion for guiding the research with his practical advice. I would also like to thank Dr. Damian Helbling who served as the minor advisor in the committee.

I am grateful to Casey Garland, William Pennock and Hui Zhi, three graduate students in the lab who helped me with the project. I am also grateful to my friends and family. Words cannot express the gratitude for their tremendous love and support.

Special thanks to Tim Brock, Cameron Willkens and Paul Charles who found solutions to technical problems with the experimental apparatus.

I would also like to thank the U.S. National Science Foundation under Award Number 1437961 for their support of the research.

TABLE OF CONTENTS

LIST OF FIGURES

LIST OF TABLES

LIST OF ABBREVIATIONS

I	the matrix of the original image pixel values
I_f	the sobel filter of the image matrix
NTU	Nephelometric Turbidity Unit
PACl	Polyaluminum chloride
ROI	Region of interest
SSE	sum of squared errors of prediction

LIST OF SYMBOLS

$A_{flowcell}$	cross sectional area of the flow cell (L^2)
A_{pixel}	projected area of particles in pixels
A_{tube}	cross sectional area of flocculator tube (L^2)
C_{Al}	Al concentration of coagulant stock (M/L^3)
C_{clay}	clay concentration added to raw water (M/L^3)
$C_{effluent}$	fraction of the effluent turbidity caused by the floc size class
$C_{influent}$	fraction of the influent turbidity caused by the floc size class
C_{plant}	Al dose within the flocculator (M/L^3)
D	inner diameter of the flocculator tube (L)
$D_{fractal}$	3-D fractal dimensión
D_p	2D fractal dimension
D_v	3D fractal dimension described by Maggi and Winterwerp
d	floc diameter (L)
d_{clay}	diameter of primary particle (L)
d_{pixel}	spherical-equivalent diameter in pixels

G	velocity gradient (1/t)
$G_{CampStein}$	velocity gradient described by Camp and Stein (1/t)
$\bar{G}$	average velocity gradient (1/t)
$\overline{G_c}$	average velocity gradient in figure eight flocculator (1/t)
$\overline{G_{Gregory}}$	velocity gradient described by Gregory (1/t)
H_{image}	depth of field (L)
k	total floc number
L_{image}	height of the image (L)
L_{tube}	length of the flocculator tube (L)
$L_{tube\ settler}$	length of tube settler (L)
l	length scale of the sobel filter kernel (L)
l_{pixel}	pixel size (L)
NA	numerical aperture
n_0	number of primary particles counted in a 2D image
n_i	number of primary particle in floc i
n_{total}	total number of primary particles within sample volume
P	power input ($M \cdot L^2/t^3$)

P_{pixel}	perimeter of flocs (in pixels)
$pC*$	removal efficiency
Q_{Al}	flow rate of coagulant solution (L^3/t)
$Q_{flowcell}$	flow rate in flow cell (L^3/t)
Q_{plant}	flow rate of the plant (L^3/t)
R	radius of the pipe (L)
R_c	diameter of curvature of the flocculator coils (L)
r	radial distance from the pipe axis (L)
S	inner width of the tube settler (L)
t	operation time (t)
V	volume of the pipe (L^3)
V_{clay}	clay volume measured according to the images (L^3)
v_0	the maximum velocity in the fluid
$v_{capture}$	capture velocity of tube settler (L/t)
v_r	velocity of fluid at a radial distance r from the pipe axis (L/t)
v_t	floc terminal velocity (L/t)
$v_{tube\ settler}$	velocity inside tube settler (L/t)

v_{up}	vertical component of the velocity in the tube settler (L/t)
$\bar{v}$	average velocity of fluid (L/t)
W_{image}	width of the image (L)
x	dimensionless floc size
α	normalized minimum pixel value
α_t	threshold value of normalized pixel value
β	dimensionless maximum floc image intensity gradient
β_t	threshold value of image intensity gradient
Δp	pressure drop along the pipe [M/(L·t^2)]
ε	average energy dissipation rate (L^2/t^3)
θ	angle of the tube settler
λ	wavelength of incident light (L)
μ	dynamic viscosity of fluid [M/(L·t)]
ν	kinetic viscosity (L^2/t)
ν_{H_2O}	kinematic viscosity of water (L^2/t)
ρ_{clay}	density of primary clay particle (M/L^3)
ρ_{H_2O}	density of water (M/L^3)

Φ	shape factor for drags on flocs

CHAPTER 1: INTRODUCTION

The quality of water has a significant impact on both human health and socioeconomic development. The criteria for access to sufficient water for domestic uses include, but are not limited to the following: safety, reliability, sustainability, affordability and physical accessibility. However, it is estimated by the United Nations (Millennium Development Goals Report, 2012) that 783 million people, or 11% of the global population, do not have access to improved sources of drinking water (such as house hold connections and public standpipes). In some rural areas, even higher portions of the population lack access to improved drinking water and are exposed to dangerous levels of biologically or chemically contaminated water due to inadequate water treatment systems. Thus, technology to provide safe water for hundreds of millions of people at low cost is in demand.

AguaClara is a multi-disciplinary program in the School of Civil and Environmental Engineering at Cornell University that conducts laboratory research leading to the design of sustainable, gravity-powered, electricity-free water treatment plants. The treatment processes include rapid mix, flocculation, sedimentation, filtration and disinfection. AguaClara designs of water treatment plants constructed in Honduras provide clean water that meets the guidelines of the World Health Organization in a cost-effective way. Ten communities consisting of 40,000 people are served by AguaClara technologies and it is anticipated that more people will benefit from this program in the near future (AguaClara, 2015).

The research in this thesis is a part of AguaClara program and it presents development of a non-intrusive imaging process as a tool for measurement of flocs formed through flocculation and clarified by sedimentation. Natural water sources contain inorganic and organic particles including pathogens, which are harmful to human health. Flocculation and sedimentation are important parts of drinking water treatment in that they can remove these particles. Flocculation is a process where colloids aggregate and form flocs that are removed by gravity forces in the sedimentation tank. However, many of the fundamental mechanisms that control flocculation are not well understood. For example, experimental data from the AguaClara research team suggests use of a mechanistic model where small particles do not readily attach to big flocs. There appears to be something about the collisions between particles that are very different in size that makes aggregation difficult. Observation of floc collisions may inform our understanding of factors that inhibit aggregation.

The objectives of this research were to develop non-destructive imaging techniques that permit floc characterization and to study the influence of coagulant dose on floc size distribution and turbidity removal. The variances in particle size distributions under different operating conditions can be of use in the understanding of aggregation mechanisms. Understanding how floc size distribution influences the flocculation process and removal of particles by sedimentation will contribute to the optimization of treatment plant design. The development of the image analysis tool also lays a foundation for future studies of particle collisions and the mechanisms that control aggregation.

CHAPTER 2: CHARACTERIZATION OF FLOCS AND FLOC SIZE DISTRIBUTION[1]

2.1 Abstract

A nonintrusive digital imaging process was developed to study particle size distributions created through flocculation and sedimentation. This process was calibrated by measuring standardized polystyrene particles of known size and was utilized to count and measure individual kaolin clay particles as well as aggregates formed by coagulation with polyaluminum chloride and flocculation. Identification of out-of focus flocs was automated with LabVIEW and used to remove them from the database that was analyzed. The particle diameter of the test suspension of kaolinite clay was measured to be 7.7±3.8 μm and a linear relationship was obtained between turbidity and the concentration of clay particles determined by imaging. The analysis technique was applied to characterize flocs and floc particle size distribution as a function of coagulant dose. Removal of flocs by sedimentation was characterized by imaging and the negative logarithm of the fraction of turbidity remaining after settling had a positive linear association with the logarithm of aluminum dose. The maximum floc size observed in the settled water was less than 120 μm, which was in accordance with the value predicted by a terminal velocity model for the capture velocity of the experimental tube settler of 0.21 mm/s.

[1]The content of this chapter will be submitted to *Environmental Engineering Science*, with co-authors M. L. Weber-Shirk and L. W. Lion.

2.2 Introduction

Flocculation facilitates aggregation of inorganic and organic particles in water sources, and is a crucial pretreatment process prior to particle removal by sedimentation and filtration. The fluid velocity gradient (G) is widely recognized as a key design parameter for laminar flow flocculators. Many studies have shown a relation between floc sizes and G (Park et al., 1972; Matsuo and Unno, 1981; Hopkins and Ducoste, 2003). Gregory (1981) and Camp and Stein (1943) proposed two different ways to calculate G, in terms of a given flow rate and tube diameter. For the conditions of this research, the average velocity gradient calculated by Camp and Stein (70.6/s) is 6% higher than that by Gregory (see calculations in Appendix A.). Energy dissipation rate (ε) is also used in the design of water treatment plants and, under conditions of laminar flow, is related to $\overline{G}$, as follows (Coufort et al., 2008):

$$\overline{G} = \sqrt{\frac{\varepsilon}{\nu}} \tag{1}$$

Where, ε is the average energy dissipation rate, and

ν is the kinematic viscosity of fluid.

During flocculation, particle sizes, structures and shapes can all affect aggregation behavior and collision efficiency (Jiang and Logan, 1991). Yao et al. (2014) reported that concentration of particles less than 5 μm is in a positive linear relationship with water turbidity in the range of 0-40 Nephelometric Turbidity Units (NTU). Nan et al. (2009) suggested that flocs in different size ranges contribute differently to the decrease in turbidity after sedimentation. Thus, the

measurement of particle size distribution during flocculation can be of use in understanding particle removal subsequent to flocculation.

Particle size characterization can be accomplished using a Coulter counter (Zhang et al., 2007) or by the electrical sensing zone method (Gibbs, 1982). However, both analyses require withdrawal of samples from a suspension that may disrupt fragile flocs (Chakraborti et al., 2000). Some researchers have adopted photographic techniques and image analysis as a non-invasive tool for the continuous measurement of changes in floc sizes in jar tests. Bouyer et al. (2004) used a laser beam as light source and VISILOG 5 for image analysis to obtain the instantaneous size distribution of flocs. However, they found it difficult to exploit the data without analyzing the contour of particles because there were too many possible intersections between the laser plane and particle shapes, and particle data needed to be discarded if the contour of the particle was shaded. PIV (particle image velocimetry) software for image acquisition and storage and NIH-Image software for image analysis have been used by Chakraborti et al. (2000) to characterize alum flocs. Keyvani and Strom (2013) developed a fully automated image processing script to remove out-of focus particles to attain more precise size distributions with Image J and MATLAB.

Based on Keyvani and Strom's study, an image analysis script was developed in this research using National Instruments LabVIEW and Vision Builder Toolkit to explore particle size distribution changes during flocculation and sedimentation. The LabVIEW software incorporates image acquisition and analysis.

2.3 Experimental Methods

2.3.1 Flocculator Setup

Figure 1 shows a schematic of the laboratory apparatus. Aerated water was pumped from a temperature-controlled reservoir and mixed with a concentrated kaolinite (R.T. Vanderbilt Co., Inc. Norwalk, CT.) clay stock to form synthetic raw water. Raw water turbidity was controlled by adjusting the flow rate of clay stock (see equation 25 in the Appendix B.) and was continuously measured using a MicroTOL 3 turbidity meter (Model number: 20055, HF Scientific, Inc. FT. Myers, FL.). The turbidity meter was equipped with a flow cell so that there was no need to withdraw samples from the raw water. Polyaluminum chloride (PACl) coagulant doses (Holland Company. Adams, MA.) ranging from (0.53 to 2.65 mg/L as Al) were mixed into the raw water. Flocculation was accomplished by laminar flow through a coiled 9.52 mm (inner diameter) tube. The average energy dissipation rate of the flocculator was 5 mW/kg and the hydraulic residence time was 300 s. Sedimentation occurred in a tube settler with a capture velocity (also referred to as a critical velocity) of 0.21 mm/s. Approximately 8% of the experimental flow could be directed to a flow cell. Two valves were utilized to control the type of water entering the flow cell allowing imaging of either flocculated water or settled water. Effluent turbidity was continuously measured using MicroTOL 2 turbidity meter (Model number: 20053, HF Scientific, Inc. FT. Myers, FL.). Process Controller software created using LabVIEW by Weber-Shirk (2008) was utilized for acquisition of turbidity data.

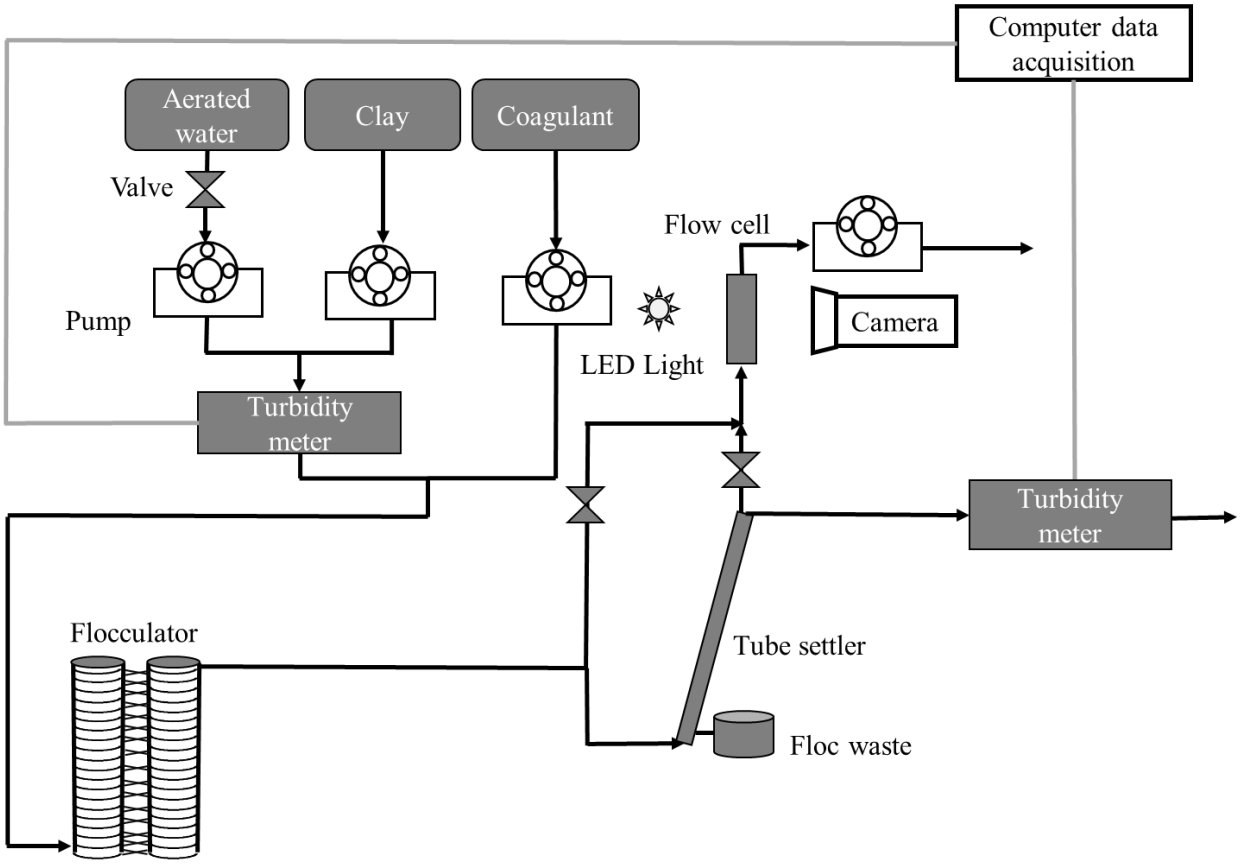

Figure 1. Schematic of the experimental apparatus.

In laminar flow, there is no turbulence to resuspend particles that may settle in the flocculator. As a result, the experimental flocculator tubing was coiled in a figure eight configuration to create a secondary flow circulation to prevent floc sedimentation (Tse et al., 2011).

The average velocity gradient ($\overline{G_c}$) in the coiled figure eight flocculator that accounts for the secondary flow was calculated as described by Tse et al. (2011):

$$\overline{G_c} = \overline{G}\sqrt{1 + 0.033\left[log\left(\frac{4Q_{plant}}{\pi D\nu}\sqrt{\frac{D}{R_c}}\right)\right]^4} \quad (2)$$

Where Q_{plant} is the experimental flow rate,

D is the inner diameter of the flocculator tube, and

R_c is the diameter of curvature of the flocculator coils.

2.3.2 Imaging system

The camera system (see Figure 2) consisted of an LED light source and a Flea3 FL3-GE-13S2M monochrome GigE camera (Point Grey Research, Inc. Richmond, BC, Canada) controlled by the LabVIEW program. The camera was a 1288×964 pixel progressive scan, monochrome 1/3" CCD fitted with an M Plan Apo 10× infinity-corrected objective lens with a numerical aperture of 0.28 (Mitutoyo Corporation, Japan). The camera can capture continuous images at up to 31 frames per second or single images by external trigger or via software control.

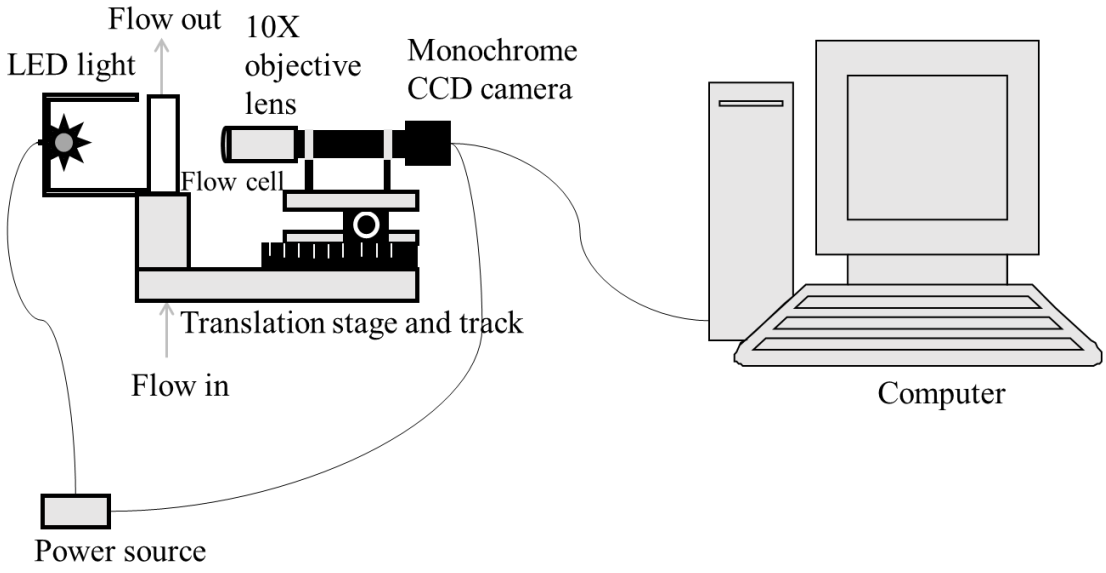

Figure 2. Imaging system consisting of LED light, CCD camera attached to a computer and the suspended sample in a flow cell.

Based on the camera sensor format and 10× magnification of the objective lens, the field of view for the imaging system was 480 μm×360 μm. Each pixel sampled an area in the field of view of 0.375 μm by 0.375 μm. The depth of field of the objective lens was calculated over a range of influent turbidities and the average value was 500 ± 90 μm (See equation (11) in part 2.6.1). The constraints for maximum floc size measurements are the field of view and the depth of field of the lens. For flocs smaller than this depth of field, it is likely that the entire floc will be in focus.

Since the size of one pixel is close to the wavelength of visible light (approximately 400-700 nm) (Pal and Pal, 2001), the diffraction of light can result in airy disks around particles in images and errors in particle size measurements. An airy disk is a bright central core surrounded by diffraction rings. More than 80% of light energy concentrates in the central ring of the airy disk (Greivenkamp, 2004), as the intensity distribution in Figure 3(A) shows.

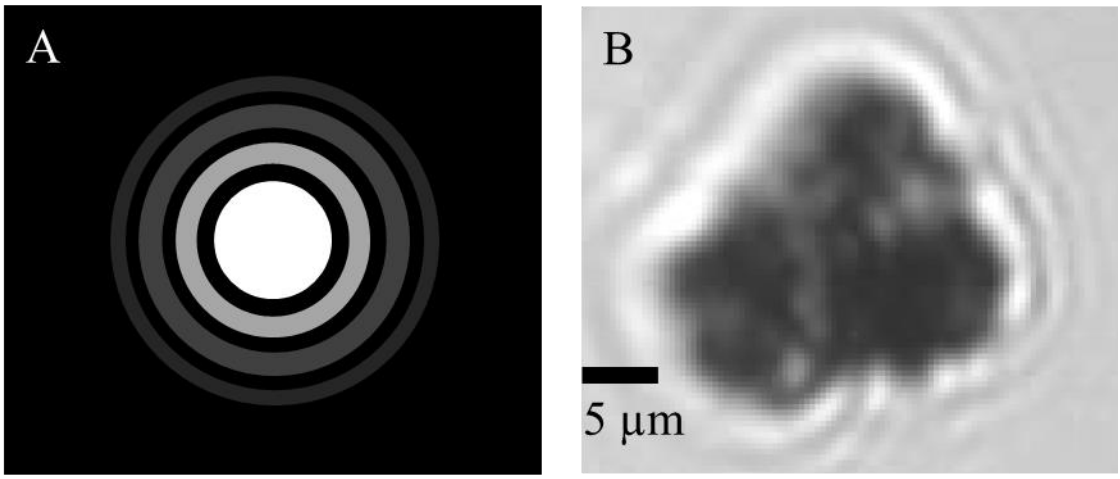

Figure 3. Airy disks. (A) Airy pattern and intensity distribution. (B) Airy patterns around a particle.

A consequence of the formation of airy disks is that a point in an object will not be imaged as a spot with sharply defined edges. Instead, it is imaged by the objective lens as a spot surrounded

by diffraction rings, which can affect the accuracy in measuring particle diameters. Figure 3(B) illustrates one example showing the airy patterns around a particle. It is obvious that the edges of the floc are not sharply contrasted.

The radius of the central ring of the airy disk can be calculated by ("Wavelength effects on performance", 2015),

$$r_{airy\ disk} = \frac{0.61\lambda}{NA} \quad (3)$$

Where λ is the wavelength of the incident light,

NA is numerical aperture, and was approximately 0.28 for the objective lens used in this research.

The estimated radius of airy disk caused by yellow light ($\lambda \approx 590nm$) is around 1.29 μm. Since each point around the particle has airy pattern, particles less than $1.29 \times 2 \approx 2.6$ μm in diameter (particle area of approximately 39 pixels) cannot be clearly identified. The apparatus could thus measure particle sizes ranging from 2.6 μm (set by the airy disk) to more than 300 μm (set by the field of view). Standardized particles of known size were utilized to determine the error in particle size measurement caused by light diffraction.

The camera was connected to the computer via Gigabit Ethernet, which allowed an acceptable transfer speed of 100 MB/s (equivalent to 2226 images of JPEG format per second). The camera was mounted on a horizontal translation stage fixed to an aluminum platform. An LED light provided bright field illumination of flocs in the flow cell (Keyvani and Strom, 2013).

The flow cell was constructed from a glass cuvette with a cross sectional area of 1 cm × 1 cm. The inlet and outlet of the flow cell had a diameter of 7.1 mm. The flow rate inside the flow cell was constrained by the minimum shutter speed of the digital camera. It was assumed that blurry images could occur when a pixel moved 1/4 of its length. Therefore, the maximum flow rate inside the flow cell was calculated by equation (4).

$$Q_{flowcell} = 0.375\ \mu m \times \frac{1}{4} \times \frac{A_{flowcell}}{t} \quad (4)$$

Where, $A_{flowcell}$ is the cross sectional area of the flow cell and t is the time the shutter is open (33 μs).

The flow rate through the sample cell was set to 0.28 mL/s based on equation (4). The average velocity gradient in the inlet port of the flow cell was 5.4/s making the average velocity gradient entering the flow cell less than 7.6% of the average velocity gradient in the flocculator. The average velocity of the water flowing through the flow cell was 2.84 mm/s. This velocity was also much higher than the sedimentation velocity of the largest flocs measured.

During initial testing of the imaging system the optimal shutter speed for image contrast was determined to be 330 μs or 10 times longer than the minimum shutter speed. The particle travel distance during this time is 1 μm and there was no evidence of significant image blurring. The 1 μm travel distance during the time when the shutter is open is small compared to the minimum particle size of 2.6 μm.

2.4 Image analysis

The image analysis script accomplished four functions: (1) reduction of image noise, (2) identification of particles from background, (3) removal of particles that were out of focus or that had portions beyond the image border, (4) calculation and recording of particle sizes. The image processing functions prepackaged in LabVIEW are capable of identifying and measuring particles. These functions include filters, threshold, basic or advanced morphology and particle analysis ("Image analysis and processing," 2008).

2.4.1 Identification of particles

A filter was first applied to each image to reduce small changes in pixel values caused by variability in the charge-coupled device of the camera. The Gaussian filtering function of the LabVIEW vision application was found to work best at reducing noise by attenuating the variations of grey scale intensity in a pixel's neighborhood. The Gaussian filter effectively smoothed the fuzzy edge of the particles in the image so that one could better extract useful information from a particular image.

Filtering was followed by the operation of thresholding, which distinguished particles from the background and produced a binary image with 0 representing the background and 1 representing particles. In general, there are two thresholding methods: global thresholding and local thresholding. Global thresholding identifies particles based on a single grayscale value. In local thresholding, each pixel is categorized based on the intensity of pixels in its neighborhood ("Thresholding," 2013). Global thresholding usually requires a specified threshold range for each

set of tests, while local thresholding can identify particles automatically. Thus, background correction ("Thresholding", 2013) within local thresholding function was utilized in the image analysis procedure in this research in that this technique is well suited for conditions where images exhibit nonuniform light intensities caused by other out of focus particles in the background.

Figure 4 shows the application of local thresholding (background correction). This local thresholding method appears to function well in particle recognition.

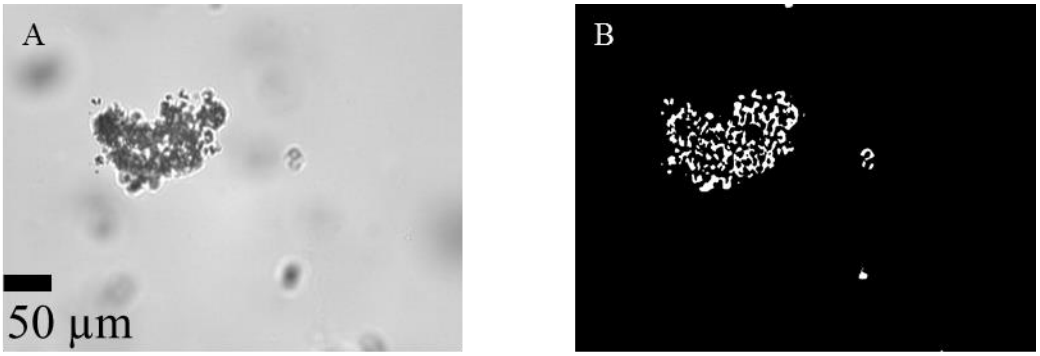

Figure 4. Application of local thresdholding. (A) The original image with flocs. (B) Local thresholding applied to image A.

When local thresholding is applied to an image, holes and gaps inside a floc can arise due to the complicated structure of the aggregates. The holes and gaps must be filled to calculate the particle area. Thus, some morphological transformations were utilized to prepare particle images for quantitative analysis. These transformations included closing the object perimeter, filling holes, and removing particles touching the border as well as small particles less than 39 pixels (equivalent spherical diameter of 2.6 µm). Particles less than 39 pixels were not considered

because they were too small to obtain an accurate measurement of their shape and area as a result of airy disc patterns.

The closing objects function was able to fill small holes and smooth the boundaries of the floc. These changes only slightly alter the shape or the area of the object. The filling holes function filled any remaining holes inside the particle boundary. Figure 5 shows an example of the morphology transformation functions.

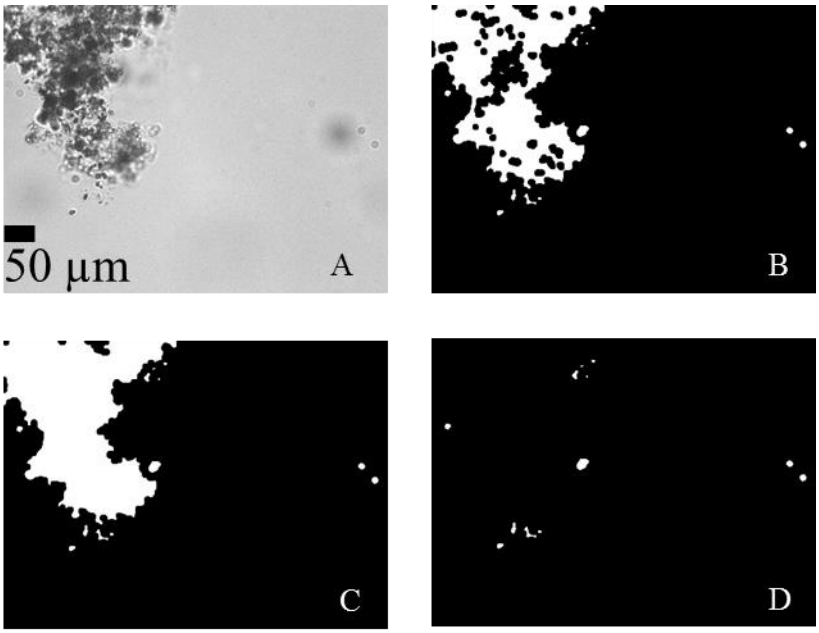

Figure 5. Example of morphological transformation. (A) Original grey scale image, (B) image after background correction and closing objects, (C) image after filling holes, (D) image after removing small particles or particles that touched the border of the image.

The next step in image analysis was to measure the area and the coordinates of the bounding rectangle of each floc in pixels. The spherical–equivalent diameter in pixels can be calculated as,

$$d_{pixel} = \sqrt{\frac{4A_{pixel}}{\pi}} \quad (5)$$

Where A_{pixel} is the projected area of the particle, in pixels. As mentioned above, particle sizes were also calibrated in this step to account for the influence of airy disks.

The Region of Interest (ROI) for each floc was defined by the coordinates of the bounding rectangle. The floc ROI of the original image was used to assess if the floc was in focus.

2.4.2 Removing out-of focus particles

As noted above, local thresholding could identify almost all particles within an image regardless of their degrees of focus, except for some extremely blurry flocs, such as the ones in Figure 4(A). Hence, the next part of the image analysis script acted to remove out-of focus flocs.

Whether an object in an image appears blurry or not is determined by its focus quality characterized by the sharp differences between background and object edges (Klinger, 2003). Keyvani and Strom (2013) introduced a concept of "clarity value" index to determine the focus quality of each floc and thus distinguish in-focus particles from the blurry ones. In their work, each image was treated with a convolution of a first Gaussian kernel in both horizontal and vertical directions. The maximum value of the filtered image associated with each floc could be used to define how close the floc was to the focal plane.

Flocs that are in focus have sharp gradients between the background and the floc. Flocs that are out of focus have weaker gradients at their boundaries. The image gradient intensity at the floc boundaries was used to eliminate flocs that were not in focus. The sobel filter computes an approximation of the image intensity gradient. High sobel filter values indicated the floc was in focus. The maximum image intensity gradient was computed for each floc. In order to eliminate

the effect of LED light intensity and shutter speed (which will have influence on the light intensity), the maximum image intensity gradient was divided by the mean pixel value of the whole image. The result was then multiplied by a length scale (3×0.375μm) related to kernel size (a kernel is a 3×3 matrix for a sobel filter) to give in a dimensionless parameter used to discriminate between in focus and out of focus flocs.

$$\alpha = \frac{\min[I(ROI_i)]}{mean[I(ROI_i)]} \tag{6}$$

$$\beta = \frac{\max[I_f(ROI_i)] \times l}{mean[I(ROI_i)]} \tag{7}$$

Where, α is the normalized minimum pixel value,

I is the matrix of the original image pixel values,

ROI_i is the bounding rectangle of floc *i*,

β is the dimensionless maximum floc image intensity gradient,

I_f is the sobel filter of the image matrix,

l is the length scale of the sobel filter kernel, which is 1.1 μm.

Darker flocs (which have smaller pixel values) were closer to the focal plane. Thus, the minimum pixel value (α) of I (the original image matrix) associated with each floc was also measured to assist in the determination of focus quality. Some transparent particles of unknown origin were observed in the clay mixture with a β greater than 0.16. These unknown particles were discarded by setting a minimum pixel value of I. The minimum pixel value of the original image was normalized to be dimensionless as described above.

Threshold values for both α and β were used to distinguish in-focus particles from those which were not in focus and were determined by examining computed values from a great number of images. After comparison, the image intensity gradient threshold value (β_t) was set to be 0.16 and the threshold value of the normalized minimum pixel value (α_t) to be 0.56. Therefore, particles with β above 0.16 and α below 0.56 were considered as in focus flocs and the remaining flocs were removed from the database. The calculated spherical-equivalent diameters of those in-focus flocs were then written to a cvs file for each image.

Figure 6 and Figure 7 are two examples showing different α and β values and the focus quality within an image.

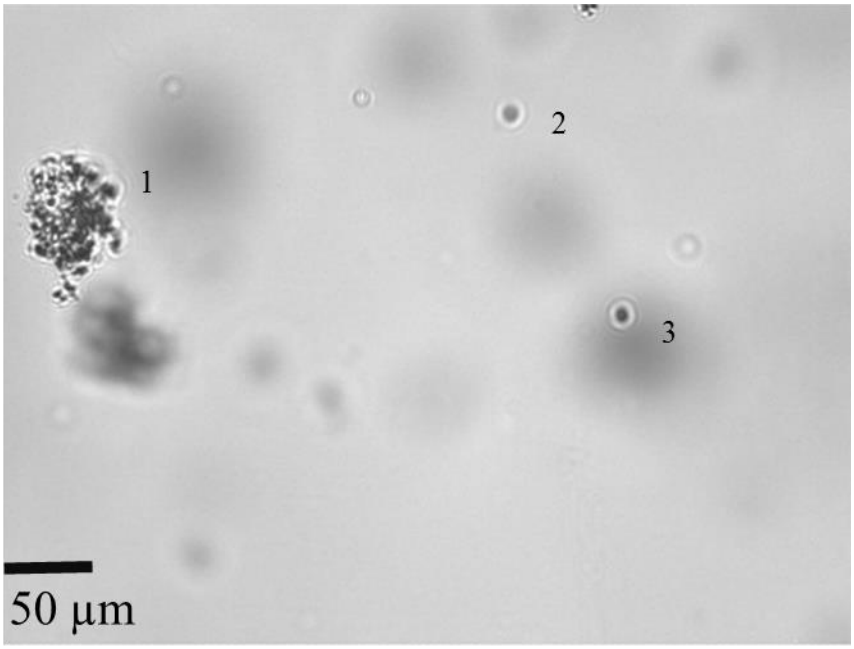

Figure 6. Sample image of identified and measured flocs.

For Figure 6, three flocs are identified after thresholding (actually four particles were identified, however one touching the top border was removed). Floc 1 has the best focus quality; flocs 2 and

3 may possibly be in-focus. As is shown in Table 1, a value of $\beta_t = 0.16$ and a value of $\alpha_t = 0.56$ worked well as a particle filter, removing the out-of focus flocs and retaining the in-focus ones.

Table 1. Identified flocs in Figure 6 with their associated α and β values. Bold values meet the constraints.

Floc number	α	β	Acceptable	Spherical diameter (μm)
1	**0.26**	**0.69**	**Yes**	56.4
2	0.65	0.15	No	---
3	**0.37**	**0.20**	**Yes**	6.9

Figure 7 is another example showing how the algorithm performed. There are seven particles detected in the image.

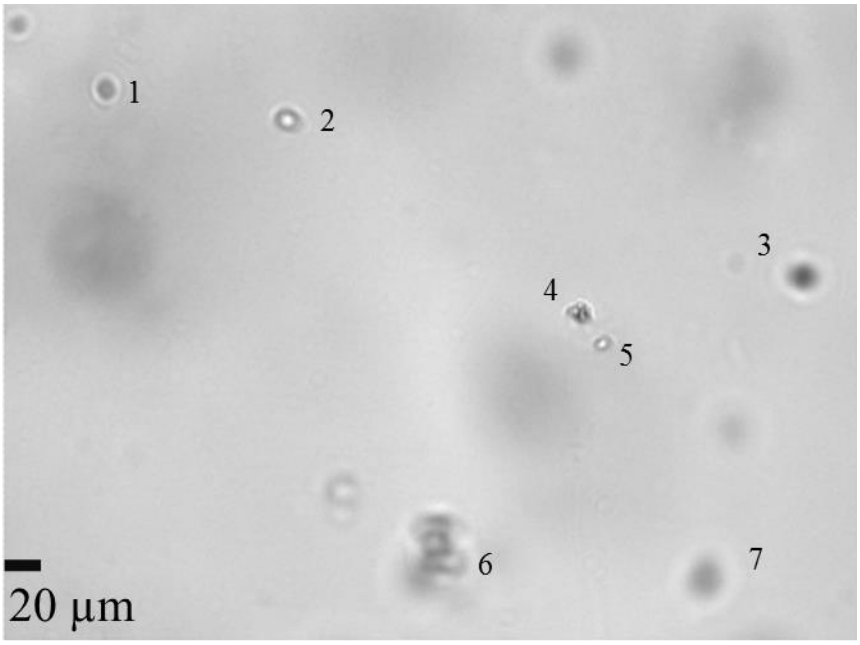

Figure 7. Sample image of identified and measured flocs.

However, by visual observation, one could easily conclude that there is only one in-focus floc (floc 4), which agrees with the result in Table 2.

Table 2. Identified flocs in Figure 7 with their associated α and β values. Bold values meet the constraints.

Floc number	α	β	Acceptable	Spherical diameter (μm)
1	0.69	0.13	No	---
2	0.69	**0.19**	No	---
3	**0.48**	0.09	No	---
4	**0.38**	**0.41**	**Yes**	11.8
5	0.74	**0.27**	No	---
6	0.66	0.08	No	---
7	0.76	0.04	No	---

Figure 8 summarizes the order of operations performed on each image to obtain the geometric characteristics of particles.

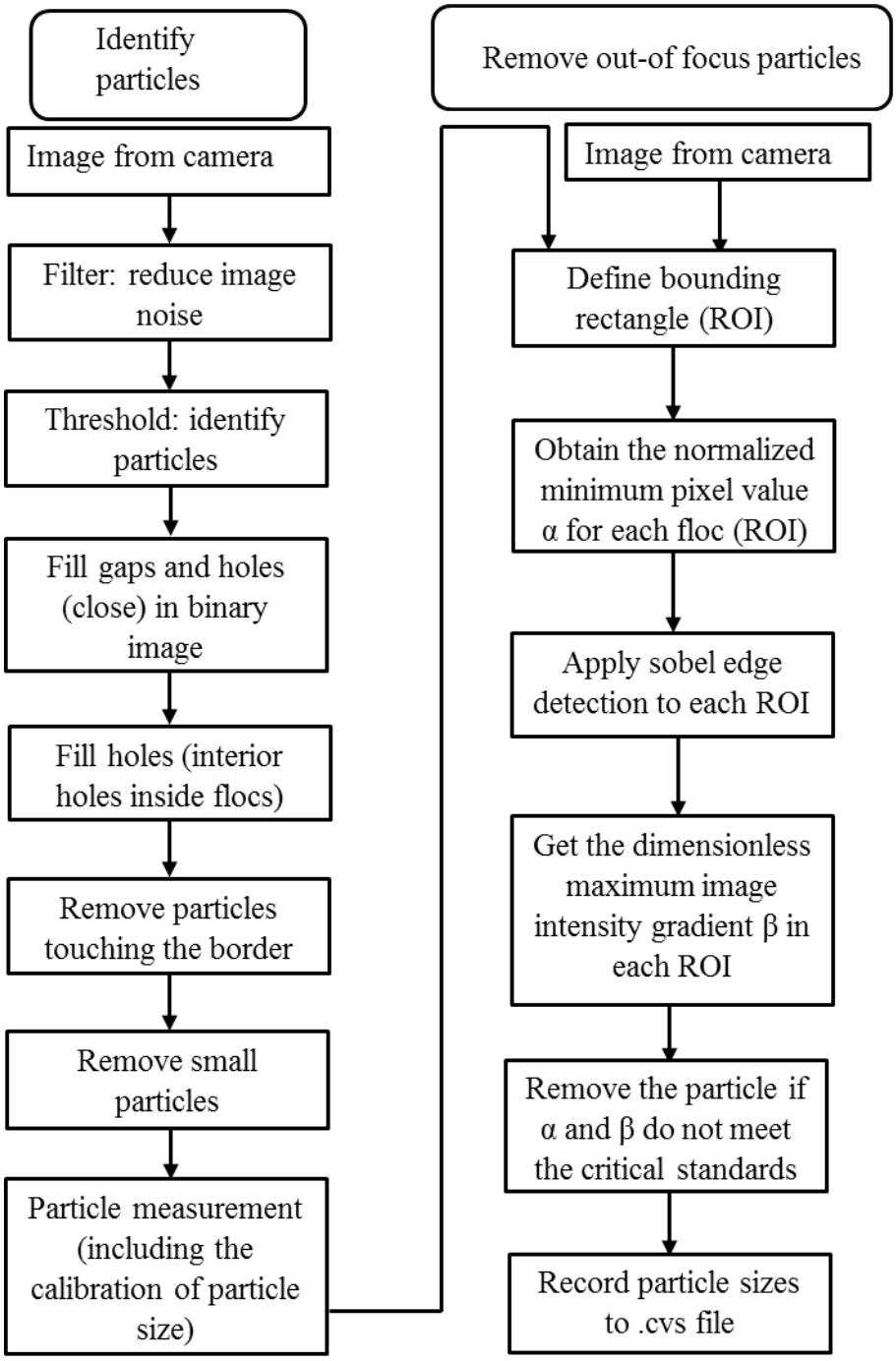

Figure 8. Flowchart of image analysis procedure.

2.5 Terminal velocity

Terminal velocity is the velocity of a floc when the forces of gravity and drag plus buoyancy are equal. Flocs are very likely to be captured by settling if their terminal velocity is higher than the capture velocity of the settling tube.

The terminal settling velocity for flocs was defined by Adachi and Tanaka (1997) as:

$$v_t = \frac{g d_{clay}^2}{18 \Phi \nu_{H_2O}} \frac{\rho_{clay} - \rho_{H_2O}}{\rho_{H_2O}} \left(\frac{d}{d_{clay}} \right)^{D_{fractal}-1} \quad (8)$$

Where Φ is the shape factor for drag on flocs, d is the diameter of floc, ν_{H_2O} is the kinematic viscosity of water, ρ_{clay} is the density of primary clay particles, ρ_{H_2O} is the density of water, d_{clay} is the diameter of the primary particles, d is the floc diameter, and $D_{fractal}$ is the 3-D fractal dimension of flocs. The shape factor accounts for the adjustment of the coefficient of drag for non-spherical geometry and has a fractional value of 45/24 (Adelman et al., 2013).

Li and Ganczarczyk (1989) calculated the fractal dimensions of the alum aggregates based on the reported data of settling tests and size-density relations. The fractal dimension from Boadway's (1978) data is calculated to be around 2.3 and the one from Tambo and Watanabe (1979) is between 1.59-1.97.

Figure 9 shows settling velocities predicted by equation (8) using a fractal dimension of 2.3.

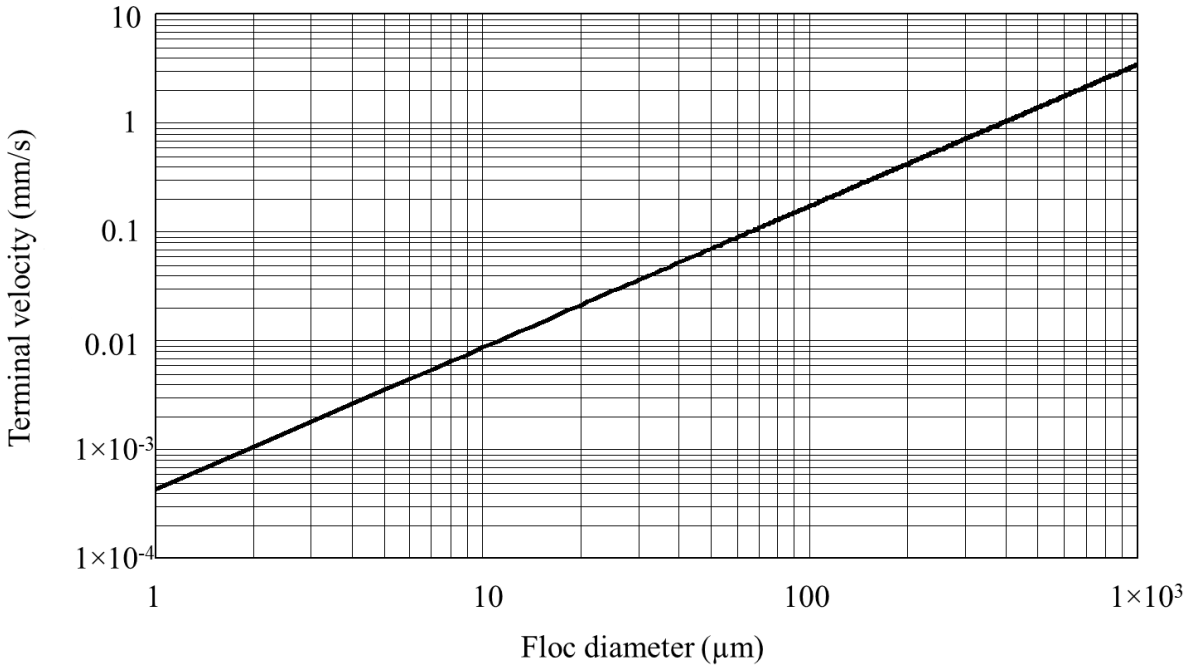

Figure 9. Terminal velocity versus floc diameter.

In the experimental tube settler the removal efficiency of slow settling flocs of a specific size can be quantified by pC*, which is defined by the following equation,

$$pC^* = -\log_{10}\left(\frac{C_{effluent}}{C_{influent}}\right) \tag{9}$$

Where, $\frac{C_{effluent}}{C_{influent}} = 1 - \frac{v_t}{v_{capture}}$ (10)

$C_{effluent}$ is the fraction of the effluent turbidity caused by the floc size class,

$C_{influent}$ is the fraction of the influent turbidity caused by the floc size class,

$v_{capture}$is the capture velocity of tube settler.

Use of the ratio of terminal settling velocity and capture velocity to quantify removal of a floc size class assumes that flocculation of particles does not occur in the tube settler. Figure 10 shows the expected pC* as a function of floc size, based on the predicted tube settler performance for the ratio of terminal velocity to capture velocity.

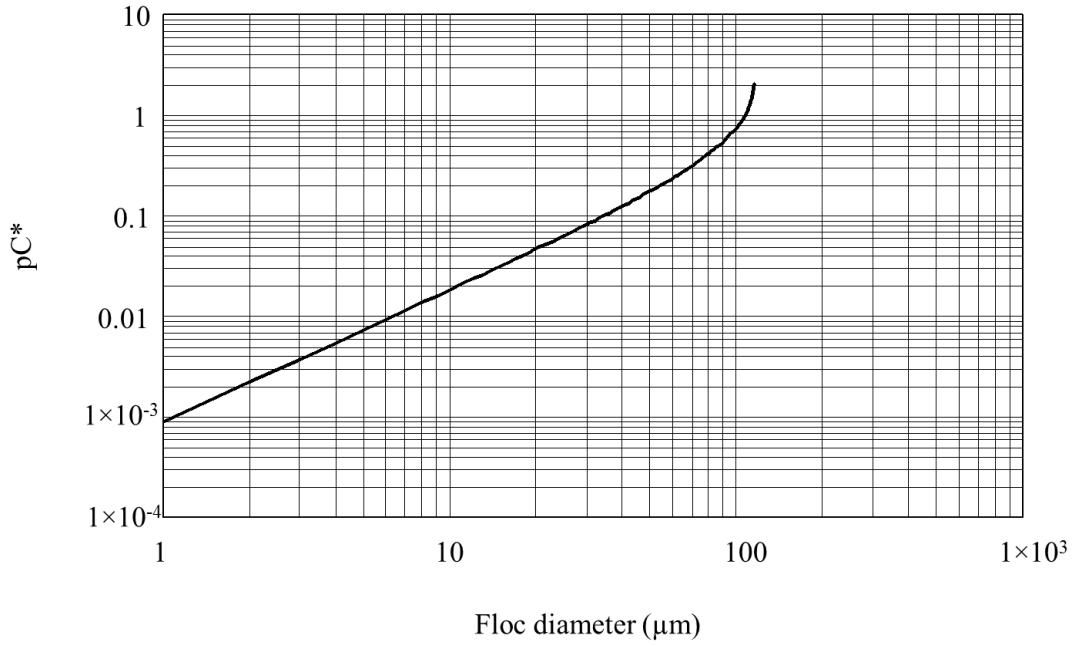

Figure 10. pC* versus floc size.

Flocs larger than 120 μm have a terminal velocity greater than capture velocity of tube settler of 0.21 mm/s, which means the removal efficiency of those flocs is expected to be 100%.

2.6 Results

2.6.1 Validation of image analysis method

The clay particle used for the test was kaolinite. Kaolinite particles have a reported diameter ranging from 0.2 μm to 12 μm (Aroke et al., 2013). The mean volume diameter of a 100 mg/L kaolinite suspension (the turbidity was 68 NTU) was measured by a Mastersizer 2000 as 7.28 μm (Wei et al., 2015). Since the size of one pixel is close to the wavelength of visible light (approximately 400-700 nm) (Pal and Pal, 2001), the diffraction of light can result in airy disks around particles in images and errors in particle size measurements.

Therefore, sizes of standardized particles were tested to determine the error caused by light diffraction in the camera setup. More than 300 images of the suspensions of dark blue polystyrene particles with nominal size of 3.0 μm (Sigma-Aldaich, Switzerland) were captured. Figure 11 is an example image of the standardized micro particles taken by the camera setup.

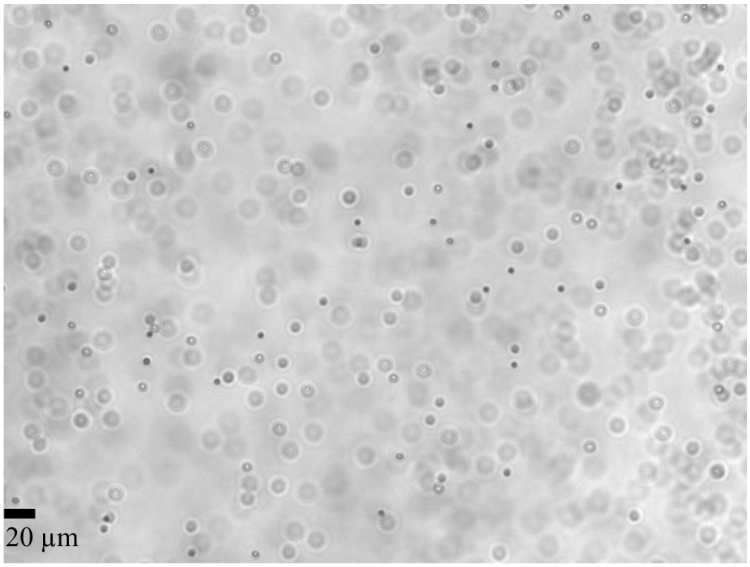

Figure 11. Image of standardized 3 µm polystyrene particles taken by the camera setup.

The images were then processed using the image analysis tool. The manufacturer determined the diameter of the standardized micro particles using a Coulter multisizer II. As is shown in Table 3, the average particle size measured by the image system was greater than the values obtained by the manufacture by 2.6 µm, which was consistent with the estimated diameter of the airy disk.

Table 3. Mean and standard deviation for 3.0 µm standardized particles

3.0 µm particles	Coulter multisizer (µm)	Image analysis (µm)
Mean	2.83	5.45
Standard deviation	0.07	1.09

The image analysis method was then used to measure the diameter of clay particles at different turbidities in the absence of coagulant, with the apparatus configured as shown in Figure 12. Based on the calibration, a correction of 2.6 µm was subtracted from the mean diameter measured by the image analysis software. Calibration of particles of larger sizes can be applied in future study to verify the accuracy of the correction value of 2.6 µm.

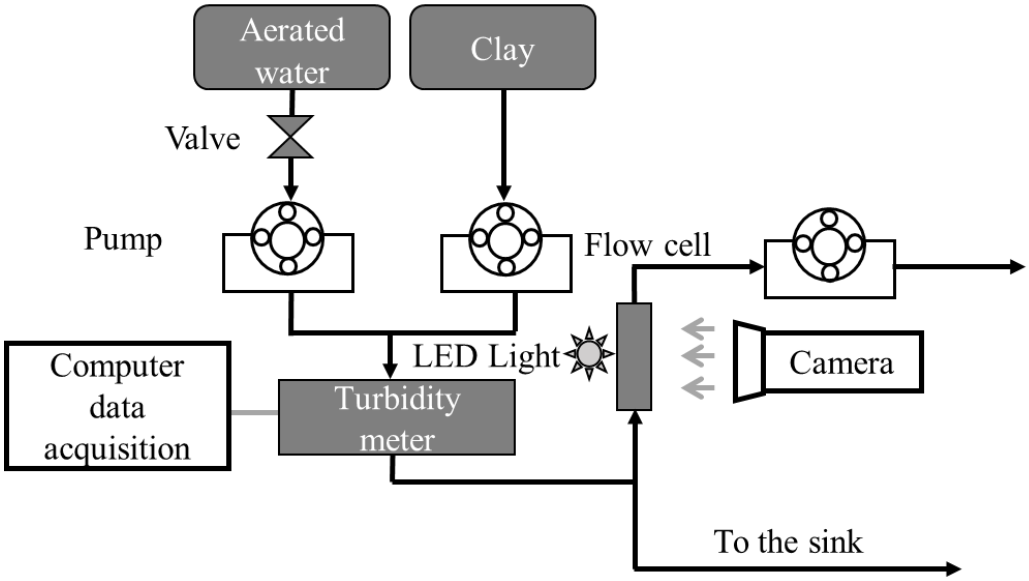

Figure 12. Schematic of experimental set up for image analysis method verification.

The average measured diameter of the test clay particles was 7.7±3.8 µm after correction for the airy disk, which was within the reported size range for kaolinite and was quite close to the mean diameter of 7.28 µm measured by Wei et al. (2015). Figure 13 illustrates the average measured clay diameters at different turbidities.

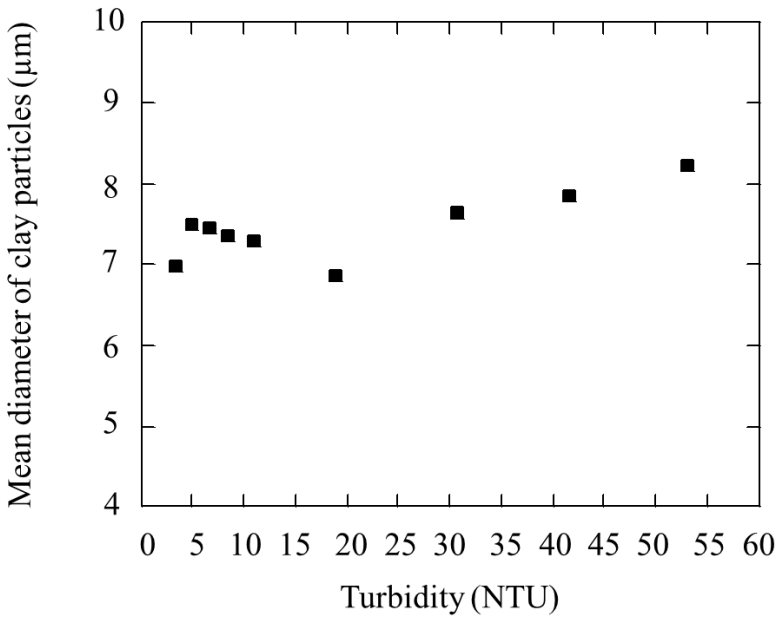

Figure 13. Average diameter of clay particles at different turbidities.

The depth of field of the lens is not specified by the manufacturer but it can be estimated. The depth of field is expected to be a function of the β_{Min} value used to identify which flocs are sufficiently in focus for further analysis.

The depth of field, H_{image}, could be derived from the following equation,

$$H_{image} = \frac{V_{clay} \cdot \rho_{clay}}{1.73 \frac{mg}{L \cdot NTU} \cdot Turbidity \cdot W_{image} \cdot L_{image}} \quad (11)$$

where W_{image} is the width of the image,

L_{image} is the height of the image,

V_{clay} is clay volume measured in one image based on the assumption that the clay particles were spheres,

ρ_{clay} is clay density and has a value of 2.5 g/cm^3,

1.73 $\frac{mg}{L \cdot NTU}$ was measured in the Cornell Environmental Engineering laboratory by Casey Garland (personal communication, June 13, 2015). This is similar to the value of 1.5 $\frac{mg}{L \cdot NTU}$ obtained by Wei et al. (2015).

The depth of field was calculated to be 500 ± 90 μm for a range of influent turbidities. For flocs smaller than this depth of field, it is likely that the entire floc will be in focus.

Figure 14 shows that there was a linear relationship between turbidity and the number concentration of clay particles based on the depth of field calculated previously.

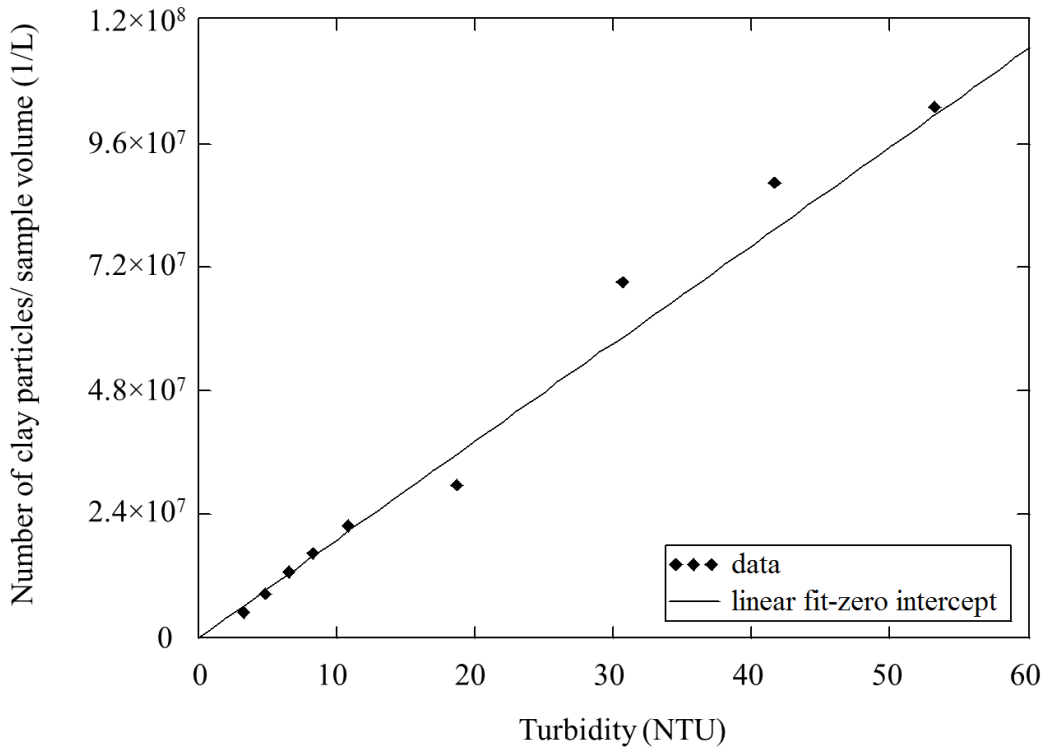

Figure 14. Number of clay particles per sample volume versus turbidity.

A linear fit with a zero intercept was obtained by calculating the average slope between each data point and the origin. The slope of the linear fit was 1.9E6 ± 2.2E5$\frac{1}{L \cdot NTU}$. Thus there were 1.9 million clay particles per $L \cdot NTU$. A $L \cdot NTU$ is equivalent to 1.73 mg of clay and given the density of clay is equivalent to a clay volume of 0.68 μL. Thus the average volume of the clay particles was 360 μm^3 which yields an equivalent diameter of 8.8 μm. This is the volume weighted average diameter of the clay particles and thus gives a slightly larger diameter then the count weighted average diameter of 7.7±3.8 μm.

2.6.2 Effect of coagulant dose

Image analysis was performed on settled water along with measurement of effluent turbidity. Figure 15 shows pC* values over a range of PACl doses. A pC* value of 1 indicates 90% removal efficiency a pC* of 2 indicates 99%, and so on. The PACl doses applied to a 50 NTU raw water were 0.53 mg/L, 1.06 mg/L, 1.59 mg/L, 2.11 mg/L and 2.65 mg/L as aluminum. As is shown in Figure 15, pC* increased when PACl dose increased and there was a linear relation between pC* and the logarithm of PACl dose.

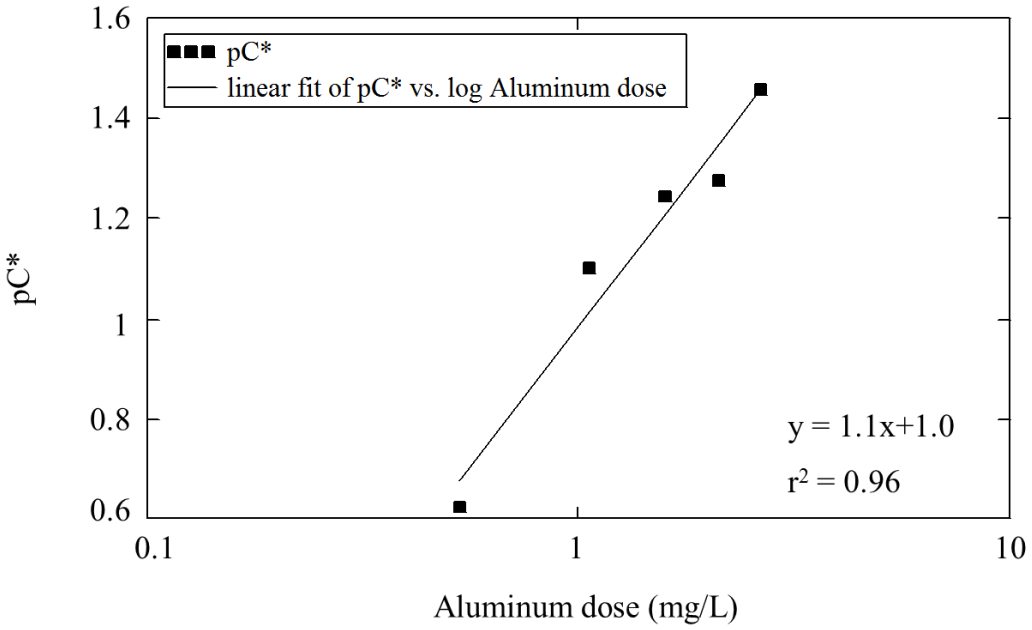

Figure 15. pC* versus PACL dose (mg/L as Al).

The result in Figure 15 agree with the flocculation model created by Swetland et al. (2014). These investigators observed a linear relationship between pC* and the logarithm of colloid surface coverage by coagulant (which is proportional to coagulant dose at low doses). The slope in Figure 15 was 1.1 and is close to the slope of 1 for the model indicated by Swetland et al. (2014).

Figure 16 illustrates the distribution of floc number concentration allocated to different bin sizes.

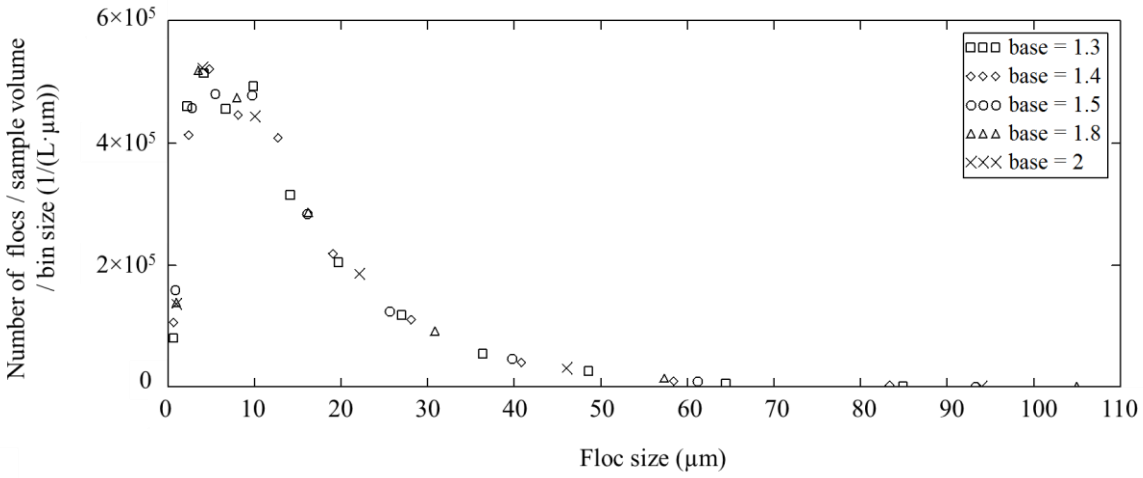

Figure 16. Floc size distributions of settled water according to different bin sizes (PACl dose = 0.53 mg/L as Al).

The horizontal axis in Figure 16 is the spherical-equivalent floc diameter while the vertical axis is the total number of flocs per sample volume per bin size within each floc size range. For each set of data, bin size was varied in a power law relation to a base. For instance, when the base is selected to be 1.3, the size of the first bin would be 1.3 µm and the first bin is defined by a lower bound of 0 µm and an upper bound of 1.3 µm, the second bin size is 1.3^2 µm (=1.7 µm) and the lower and upper bounds are 1.3 µm and 3.0 µm. The third bin is 1.3^3 µm (=2.2 µm) and its lower and upper bounds are 3.0 µm and 5.2 µm, and so on. The median value of each bin is considered as the mean diameter of flocs for that size range. The number of flocs within each bin was then counted by the LabVIEW histogram function.

For alternative bases, there were only slight changes in the shape of the distribution curve and the area under the curve. This result indicates that the specification of bin size over the range tested had little impact on the particle size distribution curve.

Figure 17 shows a log-log plot of the floc number concentration versus size. The bin sizes for each base were determined as described above. The changes in bin sizes had little influence on the log-log plot of floc size distribution.

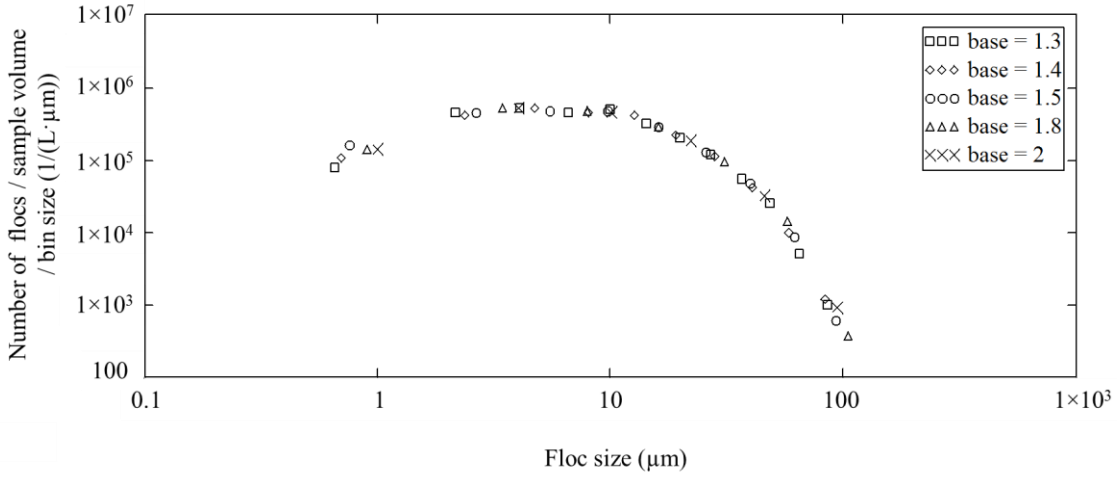

Figure 17. Log-log plot of floc size distributions of settled water according to different bin sizes (PACl dose = 0.53 mg/L as Al).

Figure 18 indicates that the number concentration of flocs in the settled water decreased with the increase in PACl dose. As is shown in Figure 9, the largest floc predicted to escape the tube settler at a capture velocity of 0.21 mm/s is 120 µm. As seen in Figure 18, the maximum floc size observed in the settled water was less than 120 µm, which is in agreement with the model.

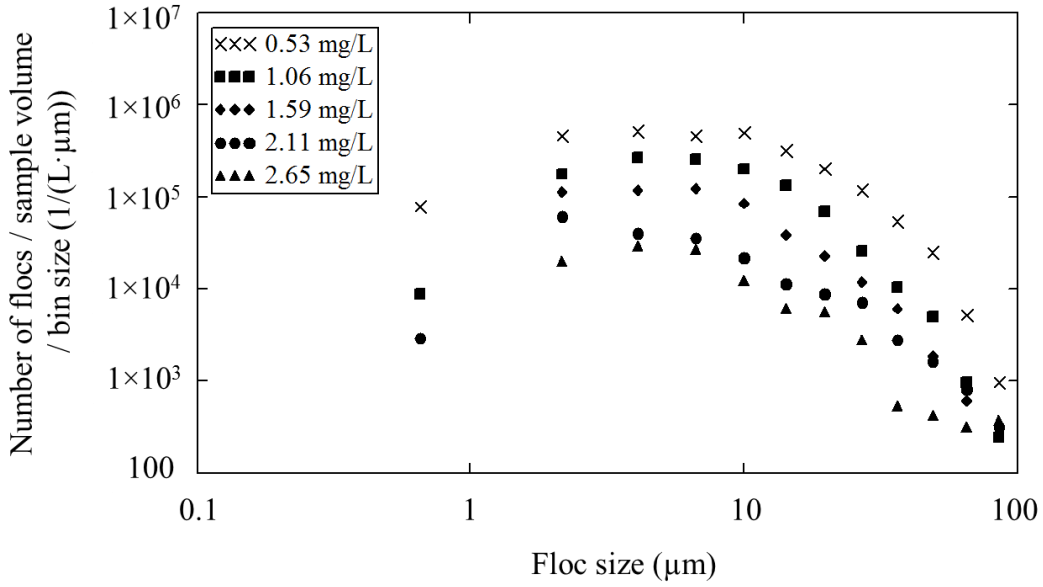

Figure 18. Floc size distributions of settled water at different PACl dose (mg/L as Al).

The data in Figure 19 suggests that the number concentration of flocs in the settled water decreases as a function of coagulant dose. Both an exponential and power law provided a good fit to the data in Figure 19. The fits to the data are shown in Table 4.

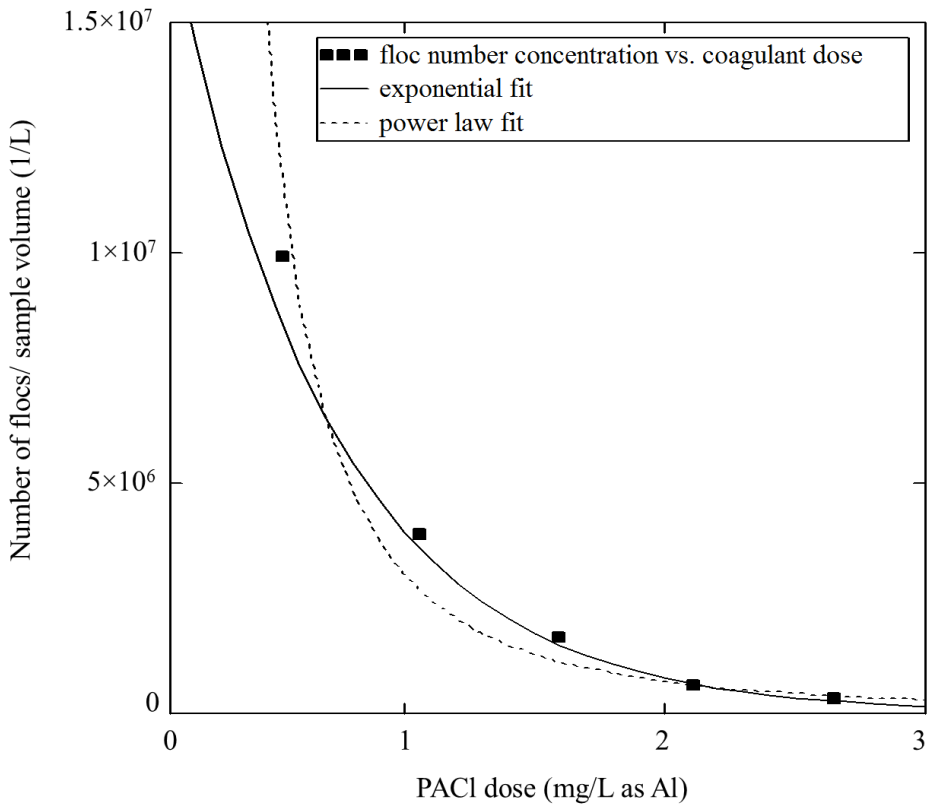

Figure 19. Floc number concentration in the settled water versus PACl dose (mg/L as Al).

At low coagulant doses, pC* had a linear relationship with the logarithm of PACl dose, indicating that turbidity and coagulant dose followed a power law relation (see Figure 15). The sum of squared errors of prediction (SSE) of exponential fit was lower than that of power law fit (see Table 4). However, it was difficult to conclude which regression better fit the data in Figure 19 because both the r squared values shown in Table 4 were quite high. Further studies over a wider range of coagulant doses (coagulant doses less than 1 mg/L as Al) should be conducted to see how floc number concentration is reduced as a function of coagulant dose.

Table 4. Exponential fit and power law fit in Figure 19.

Trend line option	Trend line equation	r^2	SSE
Exponential fit	$y = 2\times10^{7}e^{-1.6x}\frac{\mathbf{1}}{\boldsymbol{L}}$	1.00	2.3×10^{12}
Power law fit	$y = 3\times10^{6}x^{-2.1}\frac{\mathbf{1}}{\boldsymbol{L}}$	0.96	4.1×10^{12}

2.6.3 Comparison between flocculated water and settled water

In Figure 20, floc size distributions are compared between flocculated water and settled water to evaluate the performance of the tube settler. Flocculated water was sampled after the flocculator, while settled water was sampled after the tube settler.

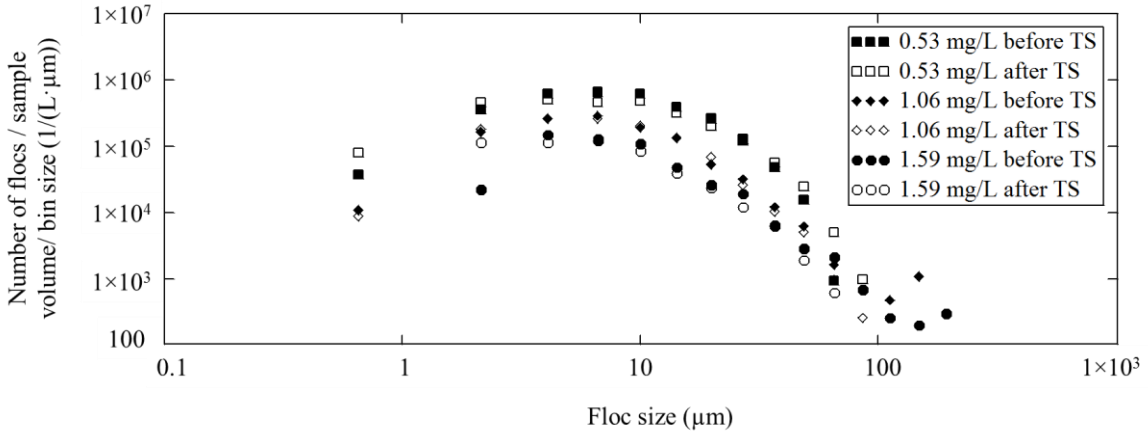

Figure 20. Size distributions of flocculated water and settled water at different PACl doses (mg/L as Al). (TS designates tube settler.)

The results confirm that sedimentation does little to remove particles below the capture velocity of the sedimentation tank. One concern with the results shown in Figure 20 is that the concentration of small flocs (less than 5 µm) in the settled water was higher than that in the

flocculated water. The inner diameter of the connecting tube between the tube settler and the turbidimeter was constrained by the 0.95 cm exit port diameter of the tube settler (see Figure 22 in Appendix. C), thus the velocity gradient inside the connecting tube was 87/s, 24% higher than that inside the flocculator. The higher shear inside the connecting tube may break big flocs into small ones. However, preferential production of floc fragments smaller than 5 μm would not be expected. Another explanation for the observed increase in small flocs might be overlapping of flocs in the depth of field within the image volume. When there is a large floc in the image, small flocs behind or in front would not be detected by image analysis. The flocculated water has more large flocs (diameter greater than 70 μm) than the settled water. Therefore, the number of small flocs in flocculated water is more likely to be under-estimated due to the image occlusion caused by big flocs. The number concentration of flocs for each bin size could possibly be corrected for occlusion by larger flocs to improve this analysis. The occluded volume would be obtained by the area of the larger flocs multiplied by the calculated depth of field.

Figure 21 shows pC* for the three coagulant doses as a function of floc sizes and the expected pC* based on predicted tube settler performance for the ratio of terminal velocity to capture velocity.

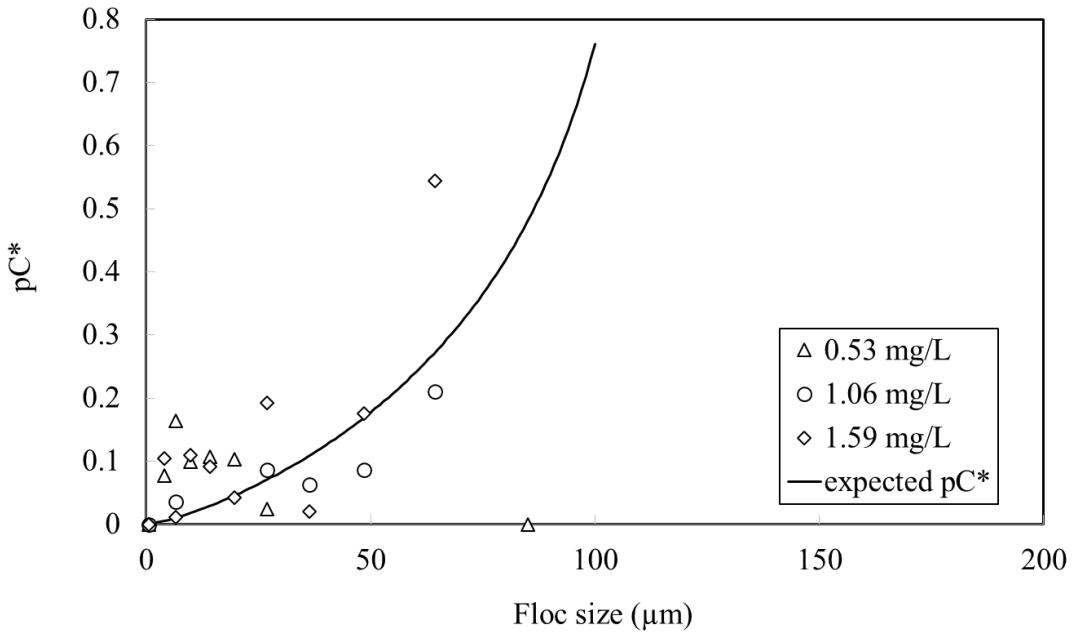

Figure 21. pC* value versus floc size.

The observed concentration changes between settled water and flocculated water were negligible (pC* of less than 0.2) except for particles that approach the capture velocity of the sedimentation tank.

2.7 Conclusions

This paper presents an effective way to employ digital image analysis to continuously count and size flocs in a flow-through-cell. Out-of focus particles are automatically identified and excluded thus improving the accuracy of the results of floc size measurement. The constraints for floc size measurements are the field of view, the depth of field and the airy patterns caused by the objective lens. The apparatus could measure particle sizes ranging from around 2.6 μm to more than 300 μm. The error in measuring particle sizes caused by airy disk (light diffraction) was

measured by testing particles of known diameter. The influence of airy disk accounted for a correction of 2.6 μm, which was consistent with the estimated diameter of the airy disk.

The average particle diameter of the test suspension of kaolinite clay was measured to be 7.7±3.8 μm and a linear relationship was obtained between turbidity and the concentration of clay particles determined by imaging.

Size distribution of flocs could be plotted in varying bin sizes, when the bin sizes increased with particle size following a power law. Since there are fewer large flocs, the bin size was kept proportional to the bin mean diameter to ensure that sufficient flocs were in the large bins to obtain a statistically meaningful particle count in each bin. Thus, varying the bin size with floc diameter can better reveal the shape of the size distribution curve. The shape and the area under the size distribution curves were independent of the bases used to set bin size.

For settled water, as was expected, floc number concentrations decreased when the PACl dose increased. pC* had a linear relationship with the logarithm of PACl dose. The maximum floc size observed in the effluent was less than 120 μm, which was in accordance with the value predicted by a model for the capture velocity of the experimental tube settler. Image occlusion caused by overlapping flocs may result in the underestimation of the number concentration of small flocs in flocculated water.

Image analysis of flocculated water could be used to predict particle counts after sedimentation. This has the potential to be used to improve performance of water treatment plants especially during raw water quality changes.

2.8 Future work

The value of α_t and β_t were determined based on looking at a range of computed α and β from large sets of floc images. The determination of α_t and β_t may be influenced by the floc image sample size (the number of floc images taken from the sample cell). In addition, the sample size may also affect the particle size distribution curve during flocculation. The study of the effect of variances in sample sizes on particle size distribution could improve the analysis.

At low coagulant doses, pC* had a linear relationship with the logarithm of PACl dose, indicating that turbidity and coagulant dose followed a power law relation. However, the relationship between floc concentration in the settled water and coagulant dose was less apparent. Both exponential and power law regressions fit the data well. In future experiments, a wider range of coagulant doses (coagulant doses less than 1 mg/L as Al) could be applied to the flocculator to check how floc number concentration is reduced as a function of coagulant dose.

The floc size distribution may follow a power law relation, $N(d) \sim d^{-p}$, where N(d) is the number of flocs per sample volume within the diameter range of d to d+Δd. The slope (-p) of the particle size distribution can vary depending on coagulation mechanisms, such as Brownian motion, fluid shear and differential sedimentation. The observations of particle size distributions in natural water sources indicate that the collision mechanisms of small (less than 2 μm) and median particles (2~60 μm) are dominated by Brownian motion and fluid shear respectively, while big flocs (greater than 60 μm) might be formed as a result of differential sedimentation (Li, et al., 2004). Thus, the change of the slopes in the floc size distribution may indicate different flocculation mechanisms for different size of particles. Future study on the slope changes may

improve our understanding of the interaction mechanisms between colloids as well as predict the evolution of floc size distribution under different operation conditions.

2.9 References

Adachi, Y., and Tanaka, Y. (1997). Settling velocity of an aluminum-kaolinite floc. *Water Res.*, 31(3), 449-454.

Adelman, M. J., Hurst. M. W., Weber-Shirk, M. L., Cabrito, T. S., Somogyi, C., and Lion, L. W. (2013). Floc Roll-up and its implications for the spacing of inclined settling devices. *Environ. Eng. Sci.*, 30(6), 302-310.

Aroke, U. O., El-Nafaty, U. A., and Osha, O. A. (2013). Properties and characterization of Kaolin clay from Alkaleri, north-eastern Nigeria. *IJETAE.*, 3(11), 387-392.

Boadway, J. D. (1978). *J. Environ. Eng.-ASCE,* 104, 901-915.

Bouyer, D., Coufort, C., Line, A., and Do-Quang, Z. (2004). Experimental Analysis of floc size distribution under different hydrodynamics in a mixing tank. *AIChE. J.*, 50(9), 2064-2081.

Camp, T. R., and Stein, P. C. (1943). Velocity gradients and internal work in fluid motion. *J. Boston Soc. Civ. Eng.*, 30, 219.

Chakraborti, R. K., Atkinson, J. F., and Benschoten, J. E. V. (2000). Characterization of Alum Floc by Image Analysis. *Environ. Sci. Technol.*, 34(18), 3969-3976.

Coufort, C., Dumas, C., Bouyer, D., and Line, A. (2008). Analysis of floc size distribution in a mixing tank. *Chem. Eng. Process,* 47(3), 287-294.

Gibbs, R. J. (1982). Floc breakage during HIAC light-blocking analysis. *Environ. Sci. Technol.*, 16(5), 298-299.

Gregory, J. (1981). Flocculation in laminar tube flow. *Chem. Eng. Sci.*, 36(11), 1789-1794.

Greivenkamp, J. E. (2004). *Field Guide to Geometrical Optics*. Bellingham, WA: SPIE Press.

Hopkins, D. C., and Ducoste, J. J. (2003). Characterizing flocculation under heterogeneous turbulence. *J. Colloid. Interf. Sci.*, 264(1), 184-194.

"Image analysis and processing." (2008). <www.ni.com/white-paper/3470/en/#toc2> (Jul.4, 2015).

Jiang, Q., and Logan, B. E. (1991). Fractal dimensions of aggregates determined from steady-state size distributions. *Environ. Sci. Technol.*, 25(12), 2031-2038.

Keyvani, A., and Strom, K. (2013). A fully-automated image processing technique to improve measurement of suspended particles and flocs by removing out-of-focus objects. *Comput. Geosci.*, 52, 189-198.

Klinger, T. (2003). *Image Processing with LabVIEW and IMAQ Vision*. Upper Saddle River, New Jersey: Pearson Education, Inc., 162-171.

Li, D., and Ganczarczyk, J. (1989). Fractal Geometry of Particle Aggregates Generated in water and wastewater treatment processes. *Environ. Sci. Technol.*, 23(11), 1385-1389.

Li, T., Zhu, Z., Wang, D., Yao, C., and Tang, H. (2006). Characterization of floc size, strength and structure under various coagulation mechanisms. *Powder. Technol.*, 168(2), 104-110.

Li, X., Zhang, J., and Lee, J. (2004). Modelling particle size distribution dynamics in marine waters. *Water Res.,* 38(5), 1305-1317.

Matsuo, T., and Unno, H. (1981). Forces acting on floc and strength of floc. *J. Env. Eng.-ASCE,* 107(3), 527-545.

Meakin, P. (1998). *Fractals, Scaling and Growth Far From Equilibrium.* Cambridge: Cambridge Univ. Press.

Nan, J., He, W., Song, X., and Lu, G. (2009). Impact of dynamic distribution of floc particles on flocculation effect. *J. Environ. Sci.,* 21(8), 1059-1065.

Pal, G., and Pal, P. (2001). *Textbook of Practical Physiology* (1st ed.). Chennai: Orient Blackswan. 387.

Parker, D. S., Kaufman, W. J., and Jenkins, D. (1972). Floc break-up in turbulent flocculation processes. *J. Sanit. Eng. Div. ASCE,* 98(1), 79-99.

Pfitzner, J. (1976). Poiseuille and his law. *Anaesthesia,* 31(2), 273-275.

Swetland, K. A., Weber-Shirk, M. L., and Lion, L. W. (2014). Flocculation-Sedimentation performance model for laminar-flow hydraulic flocculation with polyaluminum chloride and aluminum sulfate coagulants. *J. Environ. Eng.-ASCE,* 140(3), 04014002.

Tambo, N., and Watanabe, Y. (1979). Physical characteristics of flocs-I. The floc density function and aluminium floc. *Water Res.,* 13(5), 409-419.

"Thresholding." (2013). <http://zone.ni.com/reference/en-XX/help/372916P-01/nivisionconcepts/thresholding/> (Jul.4, 2015).

Tse, I. C., Swetland, K., Weber-Shirk, M. L., and Lion, L. W. (2011). Fluid shear influences on the performance of hydraulic flocculation systems. *Water Res.,* 45(17), 5412-5418.

Vahedi, A., and Gorczyca, B. (2011). Application of fractal dimensions to study the structure of flocs formed in lime softening process. *Water Res.,* 45 (2), 545-556.

"Wavelength effects on performance." (2015). <http://www.edmundoptics.com/technical-resources-center/imaging/wavelength-effects-on-performance/> (Jul. 14, 2015).

Weber-Shirk, M. L. (2008). "An automated method for testing process parameters." <http://confluence.cornell.edu/display/AGUACLARA/Process+Controller+Background> (Jul. 4, 2015).

Wei, N., Zhang, Z., Liu, D., Wu, Y., Wang, J., and Wang, Q. (2015). Coagulation behavior of polyaluminum chloride: Effects of pH and coagulant dosage. *Chinese J. Chem. Eng.,* 23(6), 1041-1046.

Xiao, F., Lam, K. M., Li, X. L., Zhong, R. S., and Zhang, X. H. (2011). PIV characterization of flocculation dynamics and floc structure in water treatment. *Colloid. Surface. A.,* 379(1-3), 27-35.

Yao, M., Nan, J., and Chen, T. (2014). Effect of particle size distribution on turbidity under various water quality levels during flocculation processes. *Desalination,* 354, 116-124.

Zhang, Z., Zhao, J., Xia, S., Liu, C., and Kang, X. (2007). Particle size distribution and removal by a chemical-biological flocculation process. *J. Environ. Sci.,* 19(5), 559-563.

APPENDIX

A. Calculation of $\overline{G}$, Q, L

Under laminar flow conditions (i.e. when the Reynolds number, $Re \leq 2100$), the velocity of fluid at a radial distance r from the pipe axis, through a straight pipe with a circular cross section, can be expressed by equation (12) (Gregory, 1981),

$$v_{r=} = v_0 \left(1 - \frac{r^2}{R^2}\right) \tag{12}$$

where, v_r is the velocity of fluid at a radial distance r from the pipe axis,

v_0 is the maximum velocity in the fluid (the axis velocity),

r is the radial distance from the pipe axis,

R is the radius of the pipe.

The average velocity of the fluid can be obtained by integrating Equation (12),

$$\overline{v} = \frac{\int_0^R v_0\left(1-\frac{r^2}{R^2}\right)2\pi r dr}{\int_0^R 2\pi r dr} = \frac{v_0}{2} \tag{13}$$

Gregory (1981) argued that the velocity gradient G at a radial distance from the pipe axis could be defined by differentiation of equation (12),

$$G = \frac{dv_r}{dr} = 2v_0 r/R^2 \tag{14}$$

G increases from zero at the pipe axis to a maximum value at the wall.

The average velocity gradient in the pipe can then be calculated as,

$$\overline{G} = \frac{2v_0}{R^2}\frac{\int_0^R 2\pi r^2 dr}{\int_0^R 2\pi r dr} = \frac{4v_0}{3R} \quad (15)$$

Since $Q = \frac{v_0}{2}\pi R^2$, (16)

$$\overline{G_{Gregory}} = \frac{8}{3}\frac{Q}{\pi R^3} = \frac{64}{3}\frac{Q}{\pi D^3} \quad (17)$$

Camp and Stein (1943) suggested that the average velocity gradient could be obtained from the power input to the volume of the pipe:

$$\overline{G} = \sqrt{\frac{P}{\mu V}} \quad (18)$$

Where, P is the power input of the system,

μ is the dynamic viscosity of the fluid,

V is the volume of the pipe.

The power input of the system could be expressed as the product of the flow rate and the pressure drop across the tube,

$$P = Q\Delta p \quad (19)$$

For a long cylindrical pipe, the Hagen-Poiseuille law (Pfitzner, 1976) leads to the calculation of the pressure drop across the pipe.

$$\Delta p = \frac{128Q\mu L_{tube}}{\pi D^4} \quad (20)$$

Where, $L_{tube}$is the length of the flocculator tube.

Combing equation (18), (19), (20) and considering $V = \pi R^2 L$, the Camp Stein expression of average G can be represented by:

$$\overline{G_{CampStein}} = \frac{16\sqrt{2}Q}{\pi D^3} \quad (21)$$

For the experimental conditions, the average velocity gradient calculated by Camp Stein (70.57/s) is 6% higher than that from Gregory.

The energy dissipation rate used in this research was: $\varepsilon = 5\frac{mW}{kg}$. The velocity gradient can be calculated by equation (1) and (2) and thus the estimated average G would be $70.6s^{-1}$. A range of Q values were substituted into equation (2) to obtain the desired experimental velocity gradient. At $Q_{plant} = 215\frac{mL}{min}$, G = 70.6 s^{-1}. When Gθ is greater than 20,000, it is expected that there would be successful flocculation in the flocculator (Camp and Stein, 1943). For safety, a Gθ value of 21,000 was selected. Hence, the residence time and the length of the tube could be separately calculated by equation (22) and equation (23), where $A_{Tube}$is the cross sectional area of the tube.

$$\theta = \frac{21000}{G} \quad (22)$$

$$L_{tube} = \theta\frac{Q}{A_{tube}} \quad (23)$$

The resulting residence time of the flocculator was 300 s and the length of the tube was 49 ft.

B. Flow rate, coagulant dose and influent turbidity

The constraints of the flow rate through the apparatus were the minimum flow rates required for the turbidity meter and the maximum rate for the flow cell. A flow rate of 3.58 ml/s through the apparatus met the minimum 1.67 ml/s requirement for the turbidity meter.

The flow rate needed for the coagulant solution was calculated by the law of conservation of mass.

$$Q_{Al} = Q_{plant} \times \frac{C_{plant}}{C_{Al}} \quad (24)$$

Where, Q_{Al} is the flow rate of coagulant solution,

Q_{plant} is the flow rate through the flocculator,

$C_{plant}$is the Al dose within the flocculator,

C_{Al} is the Al concentration of coagulant stock.

Equation (25) was used to calculate the concentration of clay added to water, the value of $1.73\frac{mg}{L \cdot NTU}$ was measured in the lab by Casey Garland (personal communication, June 13, 2015).

$$C_{clay} = 1.73\,\frac{mg}{L \cdot NTU} \cdot Target\ NTU \quad (25)$$

C. Tube settler

The 1.37 m (4.5 ft) tube settler (whose inner cross sectional dimensions are 2.22 cm×2.22 cm) has an entry port diameter of 1.3 cm (½ in) near the bottom and an exit port diameter of 0.95 cm

(3/8 in) near the top, as is shown in Figure 22. A 0.32 cm (1/8 in) diameter tap, is located on the end near to the bottom. The tap is used as a drain to remove flocs.

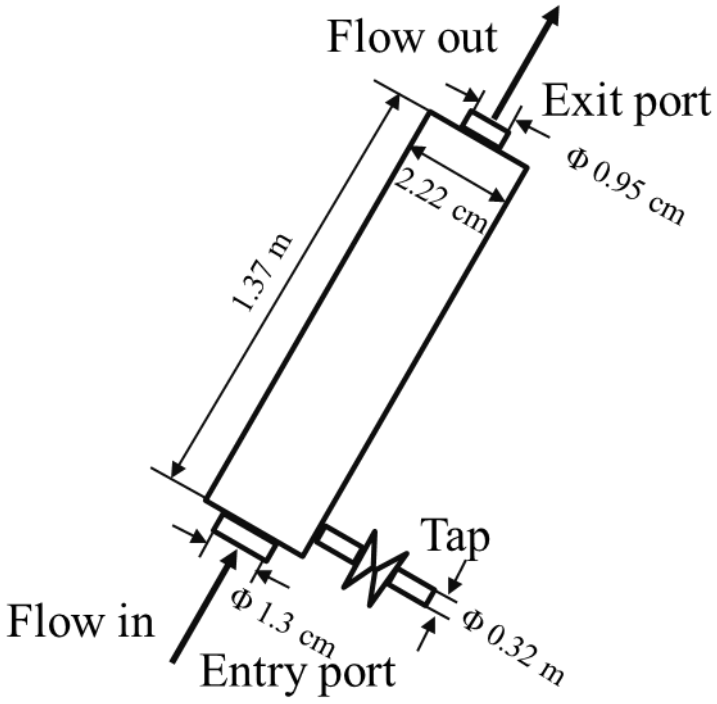

Figure 22. Tube settler.

The tube settler capture velocity was determined by following equation $v_{up}$is the vertical component of the velocity in the setting tube ($v_{tube\ settler}$) and $v_{capture}$is the capture velocity. θ is the angle of the tube settler and S is the inner width of the tube settler. $L_{tube\ settler}$ is the length of tube settler.

$$v_{up} = v_{tube\ settler} \cdot \sin\theta \tag{26}$$

$$v_{capture} = \frac{v_{up} \cdot S}{L_{tube\ settler} \cdot \cos\theta \cdot \sin\theta + S} \tag{27}$$

D. Number concentration of primary particles

The number of primary particles in each floc was calculated by the following equation,

$$n_i = \left(\frac{d}{d_{clay}}\right)^{D_{fractal}} \quad (28)$$

The total number of primary particles within sample volume can be obtained from,

$$n_{total} = \sum_{i=1}^{k} n_i \quad (29)$$

Where n_i is the number of primary particles in floc *i*,

k is the total number of flocs and $D_{fractal}$ was assumed to have the value of 2.3 reported by Li and Ganczarczyk (1989).

Figure 23 shows the estimated number of primary particles per sample volume in the effluent for each PACl dose (mg/L as Al). The straight line in the graph is the zero-intercept linear fit determined in Figure 14, which was used to predict the number of clay particles per sample volume at a given effluent turbidity. Turbidity of flocculated water was measured and turned out to be almost the same as the turbidity of raw clay water (without coagulants). Hence, the expectation was that turbidity would be related to the concentration of primary particles, meaning data points in Figure 23 should fit the relationship determined for unflocculated clay suspensions.

$$Turbidity \sim n_{total} \quad (30)$$

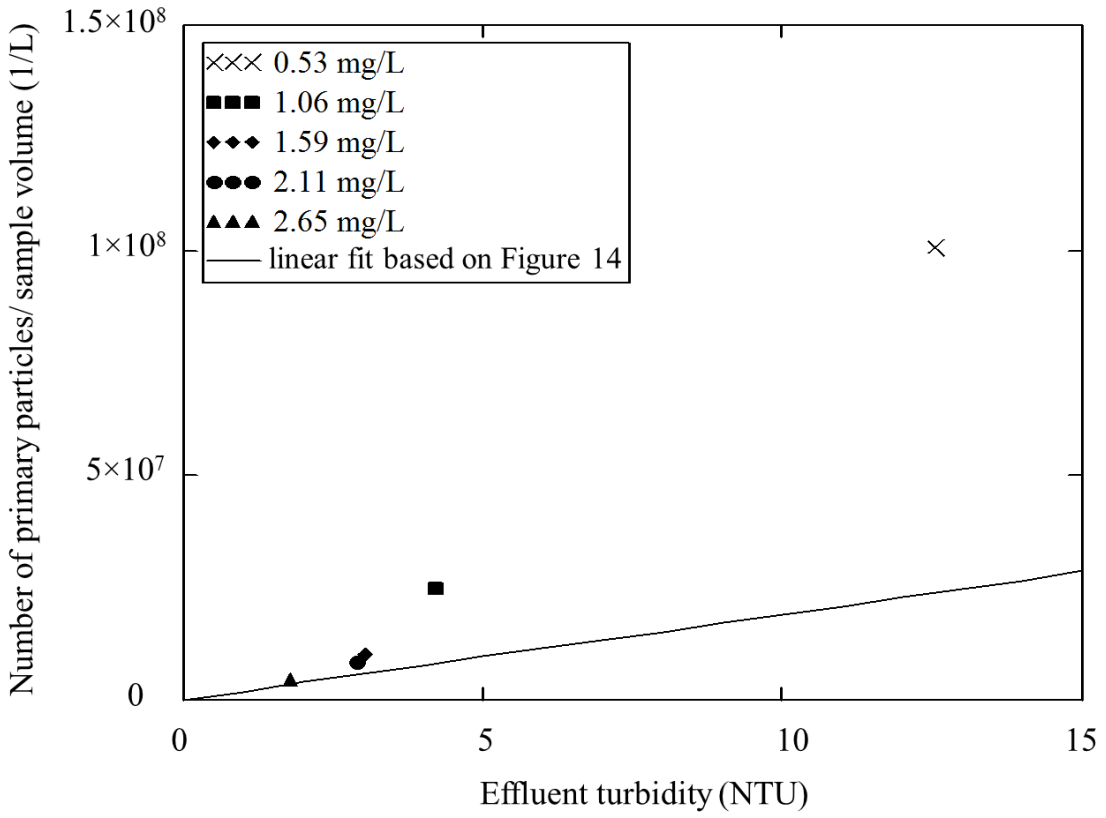

Figure 23. Estimated number of primary particles in the effluent at different aluminum doses based on an assumed fractal dimension of 2.3. Solid line is fit of number of particles per NTU based on Figure 14.

Figure 23 shows estimated primary particle number concentrations far exceeded the model. One possible explanation is that the fractal dimension of 2.3 assumed here might be incorrect. In addition, the fractal dimension can change under hydrodynamic (Li, et al., 2006) or physicochemical (Xiao, et al., 2011) conditions and has a wide range. As noted above, the reported 3-D fractal dimension of flocs have a range from 1.6 to 2.3 (Li and Ganczarczyk, 1989). Due to the power law relation, an increase in fractal dimension would result in a rapid increase in primary particle numbers.

The relationship between turbidity and primary particle number concentrations in flocs was less apparent, perhaps due to the assumption of an incorrect fractal dimension value. Further studies should be conducted on the determination of 3-D fractal dimension from 2-D floc images. This relationship will enable prediction of turbidity based on image analysis.

Figure 24 indicates that the number concentration of primary particles in the settled water decreased with the increase in PACl dose. Flocs ranging from 20 to 50 µm in diameter accounted for the greatest proportion of the primary particle concentration.

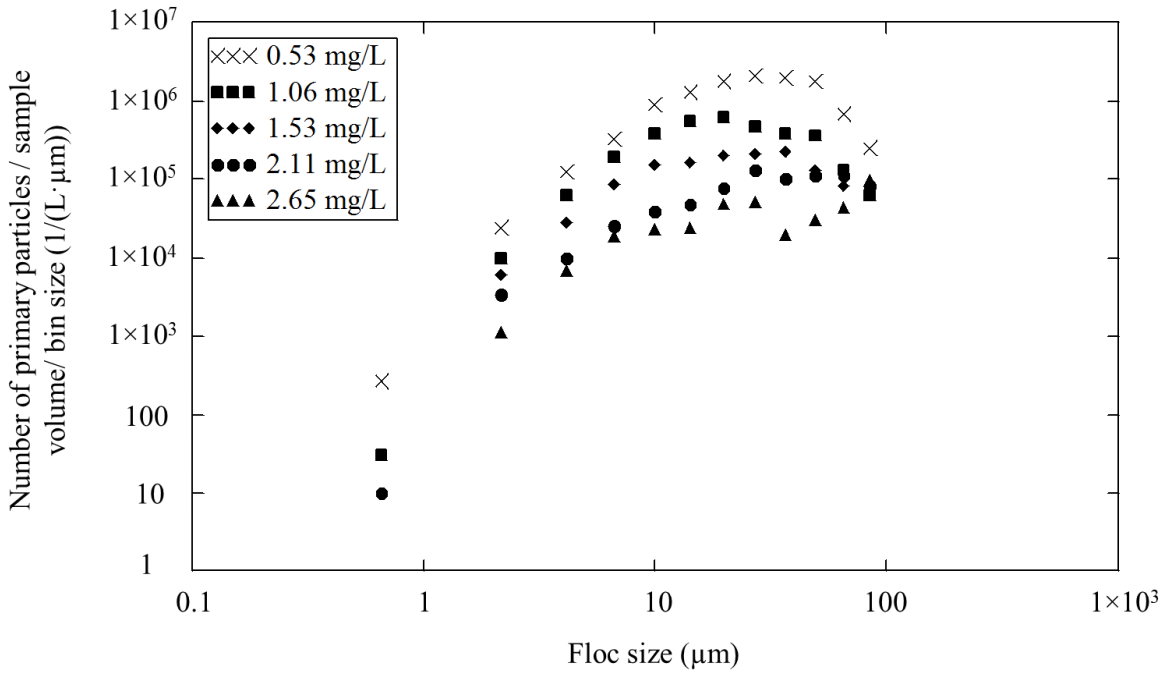

Figure 24. Primary particle distribution in the settled water at different PACL dose (mg/L as Al).

As illustrated in Figure 10, the experimental tube settler can achieve 100% removal of flocs greater than 120 µm while flocs around 68 µm would be expected to be removed with 50% efficiency in the tube settler. Thus, big flocs (greater than 70 µm) occupied a small proportion of

the mass due to their high removal efficiency. Flocs less than 10 µm account for less mass perhaps as a consequence of flocculation.

Primary particle distributions were compared between flocculated water and settled settled water to evaluate the performance of the tube settler in Figure 25. The concern in Figure 25 is the same as the one in Figure 20, as was mentioned in part 2.6.3.

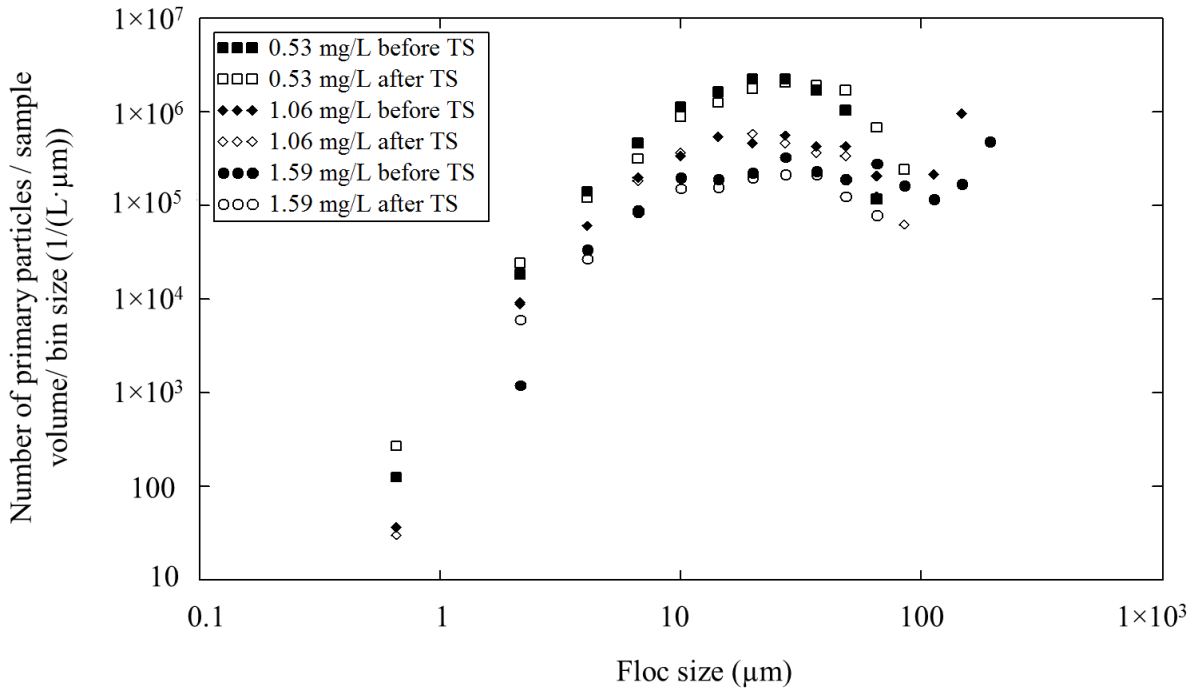

Figure 25. Primary particle distribution of flocculated water and settled water at different PACl doses (mg/L as Al). (TS designates tube settler.)

E. Fractal dimension

Fractal dimension is a crucial parameter in determining the floc shape, density, porosity, and settling velocity, as well as their kinematic behaviors, such as particle aggregation and breakup.

Numerous ways have been suggested to calculate the 3D fractal dimension. These ways include direct methods, such as a box-counting method (Vahedi and Gorczyca, 2011), and indirect methods, like a free settling test. One of the direct methods to determine the three-dimensional fractal dimension will be discussed here. This method is to relate the number of primary particles to the floc diameter (Meakin, 1998),

$$d = d_{clay} n_i^{\frac{1}{D_{fractal}}} \tag{31}$$

The number of primary clay particles in 3D dimension (n_i) could be estimated from the number of clay particles in the 2D image (n_0), based on the assumption that the flocs were spherical. Thus, the total number of primary particles in 3D dimension would be

$$n_i = \frac{4}{3}\pi\left(\sqrt{\frac{n_0}{\pi}}\right)^3 \tag{32}$$

Where, n_0 is the number of primary particles counted in a 2D image.

The fractal dimension could be then calculated by the power law fitting of equation (31).

Figure 26 shows several sample images of flocs. In terms of equation (32), the number of primary particles was counted to determine the fractal dimension of flocs. Using the graphs in Figure 26 for illustration, there were approximately twenty clay particles in the first floc. The second and third floc images have 22 and 15 clays each.

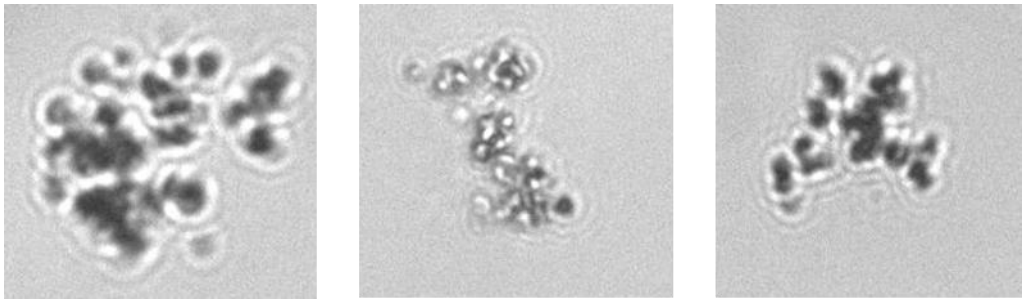

Figure 26. Sample images of flocs.

After regression analysis, the power in Figure 27 was calculated as 0.53. The 3D fractal dimension was calculated according to equation (31) and the result was approximately 1.9, which was within the range of 1.6~2.3 indicated by Li and Ganczarcayk's (1989) result. The constraint of this method is that it could only count the clay number in flocs smaller than 50 μm. For flocs larger than 50 μm, the aggregates were too densely packed to count.

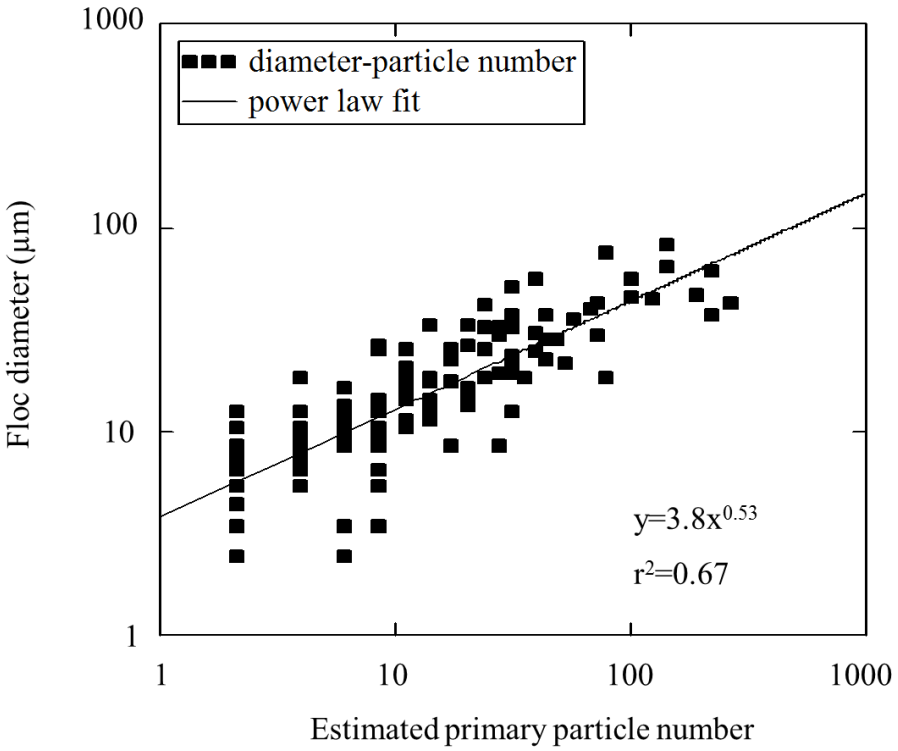

Figure 27. The regression of floc diameter vs. estimated primary particle numbers.

Maggi (2007) proposed another way to calculate perimeter-based fractal dimension. It is calculated to compare with the 3D fractal dimension attained by the power law fit of equation (31).

In Maggi's theory, the 2D fractal dimension is defined as

$$D_p = 2\frac{\log P_{pixel}}{\log A_{pixel}} \tag{33}$$

Where P_{pixel} is the perimeter of the floc while A is the projected area of the floc. Both P_{pixel} and A_{pixel} are in in units of pixels. D_p ranges from 1~2. The 3D volume fractal dimension D_v can then be derived from D_p when D_p is smaller than 2.

$$D_v = \sqrt{\frac{a(x)}{D_p - b(x)}} \quad (34)$$

Where $x = \frac{d}{l_{pixel}}$, is the dimensionless floc size, d is the floc diameter and l_{pixel} is the pixel size.

$a(x)$ and $b(x)$ are used to take the resolution into account and can be calculated from the following equations,

$$a(x) = 9[z(x) - b(x)] \quad (35)$$

$$b(x) = \frac{2[k(x)^2] - 9z(x)}{[k(x)^2] - 9} \quad (36)$$

Where $k(x) = z(x)[z(x) - 1] + 1$ (37)

$$z(x) = \frac{\log(4x-4)}{\log x} \quad (38)$$

Figure 28 shows the $D_v$calculated by equation (34).

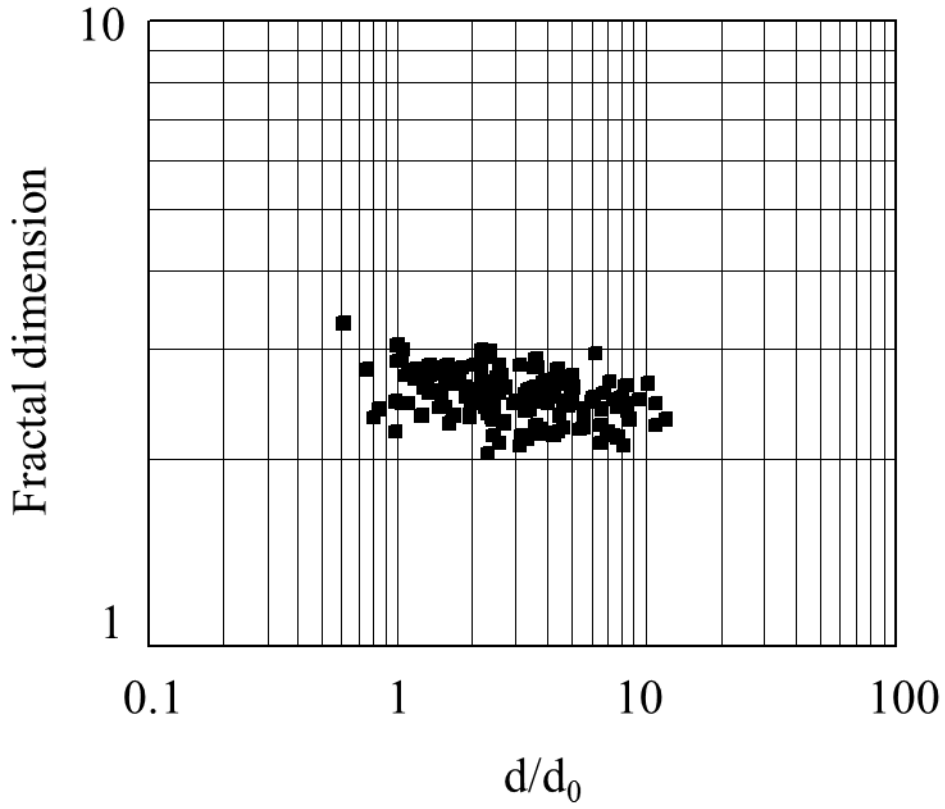

Figure 28. Volume fractal dimension of flocs.

The average fractal dimension value was 2.51 ± 0.22. The fractal dimension values are presented in the double-logarithmic plot graph. The values decreased with increasing the dimensionless size d/d_0, indicating that flocs appeared less dense and much more loosely clustered as the floc diameter increased.

REFERRENCES

Adachi, Y., and Tanaka, Y. (1997). Settling velocity of an aluminum-kaolinite floc. *Water Res.*, 31(3), 449-454.

Adelman, M. J., Hurst. M. W., Weber-Shirk, M. L., Cabrito, T. S., Somogyi, C., and Lion, L. W. (2013). Floc Roll-up and its implications for the spacing of inclined settling devices. *Environ. Eng. Sci.*, 30(6), 302-310.

AguaClara. 2015. "AguaClara Plants." < http://aguaclara.cee.cornell.edu/about/projectmap/> (Jul. 7, 2015).

Aroke, U. O., El-Nafaty, U. A., and Osha, O. A. (2013). Properties and characterization of Kaolin clay from Alkaleri, north-eastern Nigeria. *IJETAE.*, 3(11), 387-392.

Boadway, J. D. (1978). *J. Environ. Eng.-ASCE*, 104, 901-915.

Bouyer, D., Coufort, C., Line, A., and Do-Quang, Z. (2004). Experimental Analysis of floc size distribution under different hydrodynamics in a mixing tank. *AIChE. J.*, 50(9), 2064-2081.

Camp, T. R., and Stein, P. C. (1943). Velocity gradients and internal work in fluid motion. *J. Boston Soc. Civ. Eng.*, 30, 219.

Chakraborti, R. K., Atkinson, J. F., and Benschoten, J. E. V. (2000). Characterization of Alum Floc by Image Analysis. *Environ. Sci. Technol.*, 34(18), 3969-3976.

Coufort, C., Dumas, C., Bouyer, D., and Line, A. (2008). Analysis of floc size distribution in a mixing tank. *Chem. Eng. Process,* 47(3), 287-294.

Gibbs, R. J. (1982). Floc breakage during HIAC light-blocking analysis. *Environ. Sci. Technol.*, 16(5), 298-299.

Gregory, J. (1981). Flocculation in laminar tube flow. *Chem. Eng. Sci.,* 36(11), 1789-1794.

Greivenkamp, J. E. (2004). *Field Guide to Geometrical Optics*. Bellingham, WA: SPIE Press.

Hopkins, D. C., and Ducoste, J. J. (2003). Characterizing flocculation under heterogeneous turbulence. *J. Colloid. Interf. Sci.,* 264(1), 184-194.

"Image analysis and processing." (2008). <www.ni.com/white-paper/3470/en/#toc2> (Jul.4, 2015).

Jiang, Q., and Logan, B. E. (1991). Fractal dimensions of aggregates determined from steady-state size distributions. *Environ. Sci. Technol.,* 25(12), 2031-2038.

Keyvani, A., and Strom, K. (2013). A fully-automated image processing technique to improve measurement of suspended particles and flocs by removing out-of-focus objects. *Comput. Geosci.,* 52, 189-198.

Klinger, T. (2003). *Image Processing with LabVIEW and IMAQ Vision*. Upper Saddle Rive, New Jersey: Pearson Education, Inc., 162-171.

Li, D., and Ganczarczyk, J. (1989). Fractal Geometry of Particle Aggregates Generated in water and wastewater treatment processes. *Environ. Sci. Technol.,* 23(11), 1385-1389.

Li, T., Zhu, Z., Wang, D., Yao, C., and Tang, H. (2006). Characterization of floc size, strength and structure under various coagulation mechanisms. *Powder. Technol.,* 168(2), 104-110.

Li, X., Zhang, J., and Lee, J. (2004). Modelling particle size distribution dynamics in marine waters. *Water Res.,* 38(5), 1305-1317.

Maggi, F. (2007). Variable fractal dimension: A major control for floc structure and flocculation kinematics of suspended cohesive sediment. *J. Geophys. Res.,* 112(C7).

Matsuo, T., and Unno, H. (1981). Forces acting on floc and strength of floc. *J. Env. Eng.-ASCE,* 107(3), 527-545.

Meakin, P. (1998). *Fractals, Scaling and Growth Far From Equilibrium.* Cambridge: Cambridge Univ. Press.

Nan, J., He, W., Song, X., and Lu, G. (2009). Impact of dynamic distribution of floc particles on flocculation effect. *J. Environ. Sci.*, 21(8), 1059-1065.

Pal, G., and Pal, P. (2001). *Textbook of Practical Physiology* (1st ed.). Chennai: Orient Blackswan. 387. Color vision

Parker, D. S., Kaufman, W. J., and Jenkins, D. (1972). Floc break-up in turbulent flocculation processes. *J. Sanit. Eng. Div. ASCE,* 98(1), 79-99.

Pfitzner, J. (1976). Poiseuille and his law. *Anaesthesia,* 31(2), 273-275.

Swetland, K. A., Weber-Shirk, M. L., and Lion, L. W. (2014). Flocculation-Sedimentation performance model for laminar-flow hydraulic flocculation with polyaluminum chloride and aluminum sulfate coagulants. *J. Environ. Eng.-ASCE,* 140(3), 04014002.

Tambo, N., and Watanabe, Y. (1979). Physical characteristics of flocs-I. The floc density function and aluminium floc. *Water Res.,* 13(5), 409-419.

"Thresholding." (2013). <http://zone.ni.com/reference/en-XX/help/372916P-01/nivisionconcepts/thresholding/> (Jul.4, 2015).

Tse, I. C., Swetland, K., Weber-Shirk, M. L., and Lion, L. W. (2011). Fluid shear influences on the performance of hydraulic flocculation systems. *Water Res.,* 45(17), 5412-5418.

United Nations. (2012). "The millennium development goals report." <http://www.un.org/millenniumgoals/pdf/MDG%20Report%202012.pdf> (Jul. 7, 2015).

Vahedi, A., and Gorczyca, B. (2011). Application of fractal dimensions to study the structure of flocs formed in lime softening process. *Water Res.,* 45 (2), 545-556.

"Wavelength effects on performance." (2015). <http://www.edmundoptics.com/technical-resources-center/imaging/wavelength-effects-on-performance/> (Jul. 14, 2015).

Weber-Shirk, M. L. (2008). "An automated method for testing process parameters." <http://confluence.cornell.edu/display/AGUACLARA/Process+Controller+Background> (Jul. 4, 2015).

Wei, N., Zhang, Z., Liu, D., Wu, Y., Wang, J., and Wang, Q. (2015). Coagulation behavior of polyaluminum chloride: Effects of pH and coagulant dosage. *Chinese J. Chem. Eng.,* 23(6), 1041-1046.

Xiao, F., Lam, K. M., Li, X. L., Zhong, R. S., and Zhang, X. H. (2011). PIV characterization of flocculation dynamics and floc structure in water treatment. *Colloid. Surface. A.*, 379(1-3), 27-35.

Yao, M., Nan, J., and Chen, T. (2014). Effect of particle size distribution on turbidity under various water quality levels during flocculation processes. *Desalination,* 354, 116-124.

Zhang, Z., Zhao, J., Xia, S., Liu, C., and Kang, X. (2007). Particle size distribution and removal by a chemical-biological flocculation process. *J. Environ. Sci.*, 19(5), 559-563.